RICE UNIVERSITY

Plasmon Hybridization in Real Metals

by

Kui Bao

A Thesis Submitted
in Partial Fulfillment of the
Requirements for the Degree

Doctor of Philosophy

Approved, Thesis Committee:

Peter Nordlander, Chair
Professor of Physics and Astronomy;
Professor of Electrical and Computer Engineering

Naomi Halas
Stanley C. Moore Professor of Electrical and Computer Engineering; Professor of Chemistry; Professor of Physics and Astronomy

Jason Harfner
Associate Professor of Physics and Astronomy; Associate Professor of Chemistry

Houston, Texas

February, 2012

Abstract

Plasmon Hybridization in Real Metals

by

Kui Bao

By treating free electrons in metallic nanostructures as incompressible and irrotational fluid, Plasmon hybridization (PH) method can be used as a very useful tool in interpolating the electric magnetic behaviors of complex metallic nanostructures. Using PH theory and Finite Element Method (FEM), we theoretically investigated the optical properties of some complex nanostructrus including coupled nanoparticle aggregates and nanowires.

We investigated the plasmonic properties of a symmetric silver sphere heptamer and showed that the extinction spectrum exhibited a narrow Fano resonance. Using the plasmon hybridization approach and group theory we showed that this Fano resonance is caused by the interference of two bonding dipolar subradiant and superradiant plasmon modes of E1u symmetry. We investigate the effect of structural symmetry breaking and show that the energy and shape of the Fano resonance can be tuned over a broad wavelength range. We show that the wavelength of the Fano resonance depends very sensitively on the dielectric permittivity of the surrounding

media.

Besides heptamer, we also used plasmon hybridization method and finite element method to investigate the plasmonic properties of silver or gold nano spherical clusters. For symmetric clusters, we show how group theory can be used to identify the microscopic nature of the plasmon resonances. For larger clusters, we show that narrow Fano resonances are frequently present in their optical spectra. As an example of asymmetric clusters, we demonstrate that clusters of four identical spherical particles support strong Fano-like interference. This feature is highly sensitive to the polarization of the incident electric field due to orientation-dependent coupling between particles in the cluster.

Nanowire plasmons can be launched by illumination at one terminus of the nanowire and emission can be detected at the other end of the wire. With PH theory we can predict how the polarization of the emitted light depends on the polarization of the incident light. Depending on termination shape, a nanowire can serve as either a polarization-maintaining waveguide, or as a polarization-rotating, nanoscale half-wave plate. We also investigated how the properties of a nearby substrate modify the excitation and propagation of plasmons in subwavelength silver wires.

Acknowledgments

I would like to show my greatest thanks to people who have been helping me during my study. My most gratitude goes to my advisor Prof. Peter Nordlander. His persistent patience and encouragement give me courage to overcome every single difficulty I have met. His endless novel ideas lead me the way in finding new challenges and solving challenging problems. His in-depth physical view inspires me new ideas and helps touch the physical bottom of each project I worked on. His leadership is a must of the success of our group including me. Please allow me to thank my thesis committee: Prof. Naomi Halas and Prof. Jason Hafner for their valuable time in attending my thesis defense. Also, please let me show many thanks to my precious labmates: Dr. Chizuko Dutta, Dr. Daniel Brandl, Dr. Fei Le, Dr. Taeho Park, Dr. Yanpeng Wu, Dr. Feng Hao, Dr Tamer Ali, Dr Jorge Zuloaga, Mr. Heidar Sobhani, Mr. Yurong Zhen, Mr. Yang Li, Mr. Yuming Wang, Mr. Vikram Kulkarni. Their helpful discussions are very important for the success of projects. My thanks also go to The Laboratory of Nanophotonics (LANP). This platform gives me a very valuable chance to learn from other disciplines and broaden my knowledge not only in physics but also in chemistry and math. Furthermore, please allow me to express my gratitude to other collaborators, Prof. Federico Capasso, Dr. Jonathan Fan, Prof. Stefan Maier, Dr. Ai Leen Koh, Prof. Stephan Link, Mr. David Solis, Prof. Hongxing Xu, Dr. Zhipeng Li, Mr. Shunping Zhang, Prof. Mikael Kall, Mr. Vladimir Miljkovic, Prof. Dai-Sik Kim, Dr Na Liu, Prof. Naomi Halas. The pleasant discussions and

collaborations are very essential to me. Furthermore, I would like to give my great thanks to my family for their love and support. In the last, I would like to thank all the funding agencies. This work is supported by the by the Robert A. Welch Foundation (C-1222) and the National Science Foundation (CNS-0421109).

Contents

Illustrations

Chapter 1

Introduction

Although surface plasmon (SP) begins to be widely investigated scientifically in the 20th century, people have been using SP in real life since thousands of years before. In ancient times, metallic nano particles were used to color glasses, making colorful cups, potteries and windows [1, 2, 3, 4]. A very famous example is the Lycurgus cup which shows different color when light passes through the cup in different ways. People began to understand the underline physics of the optical properties of nano particles (NPs) in the 20th century after Gustav Mie's work. However, due to the limitation of experimental methods, research about SP in NPs is restrained until the end of the 20th century.

In metallic nano devices, SP is a coherent movement of surface electrons, which is a result of the interaction between dielectric and electric magnetic field of light. Thus the theoretical analysis of the behavior of SP can be done strictly by solving Maxwell equations with proper boundary conditions. To solve Maxwell equations, many numerical methods are developed including Finite Element Method (FEM) and Finite Difference Time Domain Method (FDTD).

In metallic nano devices, SP has many applications in many fields. In biomedical field, NPs' size is comparable to virus, bacteria, DNA and cells. Noble NPs are also nontoxic, which makes it possible to inject NPs into human bodies. Thus, noble

metallic NPs are used for DNA sequencing [5], cell labeling [6, 7, 8, 9], Hyperthermia treatment [10, 11] and drug delivery [11, 12, 13, 14, 15]. Here at Rice University, Naomi Halas and Jeniffer West are doing clinic tests in which gold nano shells are injected in to the blood system of mice to kill tumor cells. Gold nanoshells are silica core coated with a thin layer of gold. The size of the silica core and the thickness of the coating can be controlled such that SP resonance can be tuned over a very wide range from near ultraviolet to near infrared [16]. By delivering those gold nanoshells selectively to the tumor cells, those shells cover onto the tumor. After that, with infaraed illumination, the gold nanoshells are heated efficiently to kill the tumor cells.

In the solar energy field, people are having difficulties in enhancing the energy conversion efficiency [17]. By placing NPs into the solar cell materials, the photons are scattered efficiently due to the existence of SP. Scattered photons are trapped much longer inside the material, which causes more photons to be absorbed.

At the SP resonance, the electric filed is largely enhanced and lots of heat is generated. This makes it possible to use NPs as photocatalysis. A very promising example is the decomposition of water. At a certain high temperature, water can be decomposed into hydrogen and oxygen. Proper metallic nanoshells whose resonance are at the visible light region can be designed and put into water such that when sun light illuminates the water, those nanoshells can be heated very efficiently to a high enough temperature to decompose water. With gold NPs embedded in TiO2, Liu et

all has found that the factor of water splitting photocatalysis is increased by 66 [18].

In the information technology field, people are trying to use light instead of electricity as signal because with light as signal, the size of the device can be smaller and the ohmic loss can be minimized. SP of NPs can be used to design subwavelength optical devices such are nano antennas and nano waveguide which will be introduced in Chapter 5.

Due to such a wide range of possible applications of SP of NPs, a physical and simple model is very important to explain the behavior of SP in metal. Plasmon hybridization (PH) method treats the conduction electrons of a nanostructure as incompressible and irrotational fluid with uniform electron density. With this assumption, the behavior of SP of a nanodevice can be calculated classically without solving Maxwell equations [19]. In this thesis, we will see how PH method brings to the scientific world a simple and physical view to understand the electric magnetic properties of many complex metallic nanodevices.

The thesis will be organized as follows: In Chapter 2, we will generally introduce the basics of PH theory. In Chapter 3, we use the FEM method to numerically calculate the optical properties of a nanostructure called heptamers. PH method and group theory are used to interpolate the simulation results. In Chapter 4, we extend our nanostructure to many different kinds of aggregates of nanoparticles. FEM method is used to do the numerical analysis. Group theory and PH method are used to do the theoretical analysis. In Chapter 5, we use PH method to explain how the

plasmon energy propagates and decays along a gold nano wire with different radius, tip shape, distance from the substrate and permittivity of the substrate. Finally, the conclusions of the thesis are in Chapter 6.

Chapter 2

Plasmon Hybridization method

2.1 Introduction

The field of nanoparticle plasmonics is rapidly becoming one of the major research fields in nanoscience. The optical properties of a metallic nanostructure are determined by their local surface plasmon resonances (LSPR) which are collective oscillations of their conduction electrons. For resonant excitation of LSPR, intense local electric fields can be induced at the nanoparticle surfaces, a property that can be exploited in surface enhanced spectroscopy (SES) applications such as surface enhanced Raman scattering Petschulat et al. [20], Chen et al. [21], Liang et al. [22], Mu et al. [23], Ochsenkühn et al. [24].The LSPRs are strongly dependent on the shape and composition of the nanostructure and are thus highly tunable Yang et al. [25], Encina and Coronado [26], Ye et al. [27], Tserkezis et al. [28], Zhu [29], Netzer et al. [30]. This tunability is crucial for the development of SES substrates where intense hotspots at wavelengths relevant for molecular excitations and available lasers are needed.

A variety of computational tools have been developed and successfully used for the electromagnetic modeling of nanostructures Chremmos [31], Khoury et al. [32], Teperik and Borisov [33], Chau et al. [34], Montgomery et al. [35]. The PH method is another powerful method that provides analytical electromagnetic solutions for

highly symmetric nanostructures in the quasistatic limit Prodan et al. [36]. The PH method expresses the plasmon modes of a complex nanostructure in terms of interactions between the plasmon resonances of its elementary components. The resulting hybridized plasmon modes are formed in rigorous analogy with molecular orbital formation from atomic orbitals in molecular orbital theory. The PH concept provides a simple and intuitive understanding of how the plasmon resonances of a composite nanostructure depend on the plasmon modes of its individual components, and has been widely used by many groups Liu et al. [37, 38], Moradi [39], Yuan and Gao [40], Yang et al. [41]. In the following section, we will go through the basics of PH theory, for more details, please check Prodan and Nordlander [19].

2.2 The plasmon hybridization method: Drude model

In the PH method, the conduction electrons of a nanostructure are treated as an incompressible fluid of uniform electron density n_0 confined to a uniform positive background of dielectric permittivity ε_∞. We will here describe the method only briefly, and refer the reader to the original work for more details Prodan and Nordlander [19].

Incompressible deformations of a liquid can be described by their velocity fields $\vec{v}(\vec{r})$ which denote the velocity of a volume element of the liquid at position $\vec{r}$. Incompressible deformation fields can conveniently be expressed as gradients of scalar potentials that satisfy Laplace equation. In a given geometry, one can trivially find

a complete set of such scalar potentials $\phi_\mu(\vec{r})$ where μ is an index that labels the individual basis functions. For instance in a spherical geometry for an individual particle, μ would be equal to the multipolar indices (l, m), and for a planar geometry, μ would be the parallel wave vector.

An arbitrary incompressible deformation of the conduction electron liquid in a multiparticle structure can thus be written as

$$\vec{v}(\vec{r}) = \sum_{i\mu} \frac{d}{dt} A_{i\mu}(t) \nabla \phi_{i\mu}(\vec{r}) \tag{2.1}$$

In this expression we refer to $|i\mu>$ as a primitive plasmon mode μ on nanoparticle i with an associated velocity field$\vec{v}_{i\mu}(\vec{r})$=$\nabla\phi_{i\mu}(\vec{r})$and a time dependent amplitude $\frac{d}{dt}A_{i\mu}(t)$. For simplicity, in the following we will incorporate the particle index i into μ.The primitive plasmon amplitude $A_\mu(t)$ describes the spatial displacement of the primitive plasmon $|\mu>$. Since the electron liquid is incompressible, only surface charges can result from the deformations. Each primitive plasmon mode $|\mu>$induces a surface charge that can be determined from the continuity equation:

$$\sigma_\mu(\vec{s}, t) = -n_0 e A_\mu(t) \nabla \phi_\mu(\vec{s}) \cdot \hat{s} \tag{2.2}$$

where $\vec{s}$ is a point on the surface of the nanostructure and $\hat{s}$ is its normal unit vector in the outward direction from the metal surface.

In the presence of metallic background polarizabilities ε_∞ and any other back-

ground dielectrics such as embedding media or dielectric particles or layers, extra screening charges will be induced on the surfaces of the nanostructure. The resulting screened surface charge distribution $\tau_\mu(\overrightarrow{r})$ originating from the primitive plasmon mode μ depends on its amplitude and the dielectric permittivities of the background materials.

In a complex geometry such as a multiparticle aggregate or a nanoparticle with multiple disconnected surfaces, the primitive plasmon modes can interact with each other through the Coulomb potential and are no longer the eigenmodes of the system. For small amplitude motion, all interactions are linear. To obtain the normal modes, one assumes that all modes move harmonically, and look for self sustained solutions, i.e. finite amplitude modes that exist without an applied external field. The kinetic and potential energies of the primitive plasmons can be calculated directly from their velocity fields $\vec{v}_\mu(\overrightarrow{r})$ and screened surface charge distributions $\tau_\mu(\overrightarrow{r})$.

The potential energy of the system will contain nondiagonal elements resulting from the interaction of primitive plasmon modes of different μ. By constructing and diagonalizing the Lagrangian for the system, the new eigenmodes can be determined. These hybridized eigenmodes are superpositions of the individual primitive plasmon modes.

The optical absorption of the nanostructure is calculated directly from the equation of motion for the system in the presence of an external electric field. For a nanoparticle in the quasistatic limit, i.e. much smaller than the wavelength of the

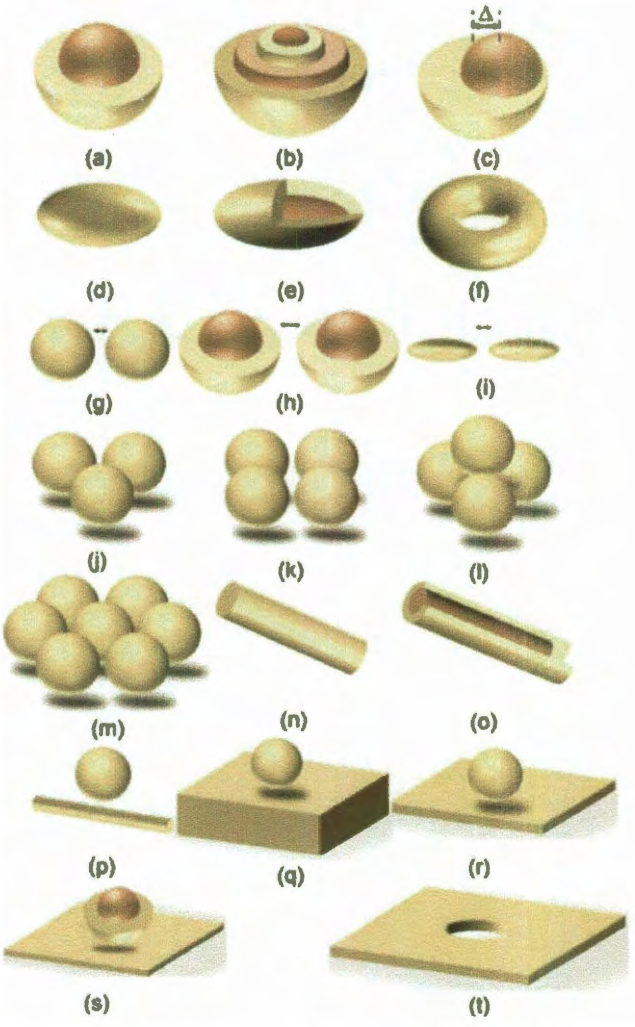

Figure 2.1 : Schematics of geometries where the PH method has been applied. (a) Nanoshell and (b) nanomatryushka [19]; (c) nanoegg [42]; (d) prolate or oblate spheroids [43]; (e) nanorice [43, 44]; (f) nanotorus [45]; (g) nanosphere dimmer [46]; (h) nanoshell dimmer [47]; (i) nanorod dimmer [48]; (j) nanoparticle trimer and (k) quadrumer [49]; (l) nanoparticle tetramer [50]; (m) nanoparticle heptamer [51]; (n) solid and (o) dielectric core-shell nanowires [43]; (p) nanoparticle interacting with a metallic wire [52]; (q) nanoparticle interacting with a semi-infinite metallic surface [53]; (r) nanosphere interacting with a thin metallic film [54]; (s) nanoshell interacting with a thin metallic film [55]; (t) cylindrical hole in a thin metallic film [56]. Metallic materials are illustrated in yellow and dielectrics in brown.

incident light, only plasmon modes with finite dipolar components will couple to the incident field. The optical absorption can be expressed in terms of the frequency dependent dipolar polarizability $\alpha(\omega)$ of the nanostructure as

$$\sigma(\omega) = \frac{\omega}{c} Im[\alpha(\omega + i\delta/2)] \tag{2.3}$$

where δ is a damping parameter and c is the speed of light. The damping parameter describes the dissipation (friction) in the system and results in a broadening of all the modes. By choosing the damping to correspond to the damping in real metals, the calculated absorption spectra agree perfectly with exact calculations. However, in many applications it is convenient to use a very small damping to better resolve the individual hybridized plasmonic modes.

Since the PH method is a microscopic approach, it does not explicitly require a dielectric permittivity of the metal as an input. However, for a conduction electron liquid of uniform density n_0, the resulting bulk dielectric function is of the Drude form:

$$\varepsilon(\omega) = \varepsilon_\infty - \frac{\omega_B^2}{\omega(\omega + i\delta)} \tag{2.4}$$

In this expression the bulk plasmon frequency is

$$\omega_B = \sqrt{\frac{4\pi n_0 e^2}{m_e}} \tag{2.5}$$

where m_e is the effective mass of a conduction electron.

The Drude model eq. (4) has three parameters: ω_B, ε_∞ and δ. For the coinage metals Ag and Au, for wavelengths longer than 500 nm, one can find fixed parameters that provide an accurate modeling of the experimentally determined dielectric data by Johnson and Christy (JC) Johnson and Christy [57]. Using such dielectric descriptions, the PH method has successfully been applied to a wide variety of geometries as illustrated in Figure 2.1.

In the next section, we show how one can introduce frequency dependent parameters ω_B, ε_∞ and $\delta(\omega)$ in the PH method and model metals of arbitrary dielectric permittivities.

2.3 The plasmon hybridization method: Realistic metal dielectric function

The optical response of a nanoparticle is determined by its real and imaginary dielectric permittivities. The real part determines the shift of the plasmon resonances and the imaginary part determines the width of the modes. Using a correct imaginary part is particularly important for the electromagnetic field enhancements. A decrease of the damping δ by an order of magnitude translates into an order of magnitude increase of the enhancements. In many tables and reference works, experimental dielectric data is parameterized in terms of the real and complex refractive indices $n(\omega)$ and $k(\omega)$ which are related to the complex dielectric permittivity as

$$\varepsilon(\omega) = [n(\omega) + ik(\omega)]^2 \tag{2.6}$$

The material parameters that are required in a PH calculation are the background polarizability ε_∞, the damping δ and the conduction electron density n_0 which enters the Lagrangian indirectly through the bulk plasmon energy ω_B. To fit the real and imaginary part of the permittivity to a realistic dielectric permittivity such as JC, we introduce frequency dependent parameters ω_B, ε_∞ and $\delta(\omega)$ in eq. (4) and obtain for the real part

$$\varepsilon_R(\omega) = Re[\varepsilon(\omega)] = \varepsilon_\infty(\omega) - \frac{\omega_B^2(\omega)}{\omega^2 + \delta^2(\omega)} \tag{2.7}$$

and for the imaginary part

$$\varepsilon_I(\omega) = Im[\varepsilon(\omega)] = \frac{\omega_B^2(\omega)\delta(\omega)}{\omega(\omega^2 + \delta^2(\omega))} \tag{2.8}$$

For each frequency, there are two equations and three unknowns. Thus the parameters are not determined unambiguously. If one parameter is fixed, the other two can be determined directly from eqs. (7) and (8).

Figure 2.2(a) shows the absorption spectrum of a silver nanosphere dimer calculated using completely different parameterizations of the JC data. The two prominent peaks are the hybridized bonding dipolar ($l = 1$) and quadrupolar ($l = 2$) dimer resonances. The higher energy quadrupolar mode is visible because the hybridized

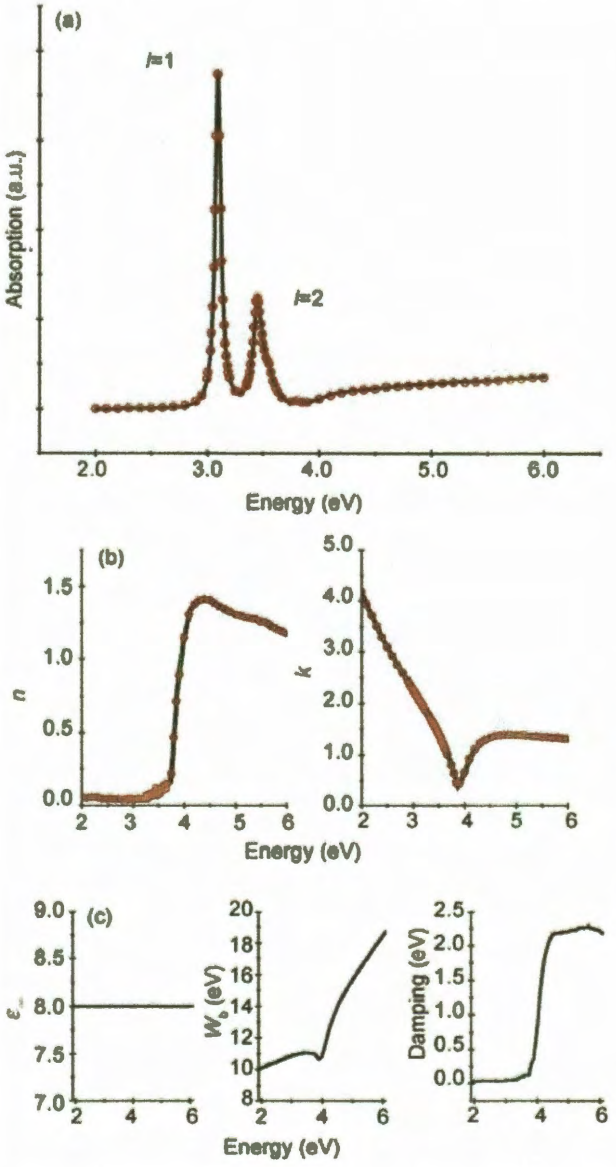

Figure 2.2 : (a) Absorption spectra for an Ag nanosphere dimer calculated using PH for two different parameterizations of Ag JC data: (black) fixed $\varepsilon_\infty = 8$; (red) random ε_∞. The radii of the Ag spheres are 10 nm and the interparticle separation is 1 nm. (b) Real and complex refractive indices for the two different parameterizations of the JC data. (c) Frequency dependence of ω_B and $\delta(\omega)$ for the fixed $\varepsilon_\infty = 8$ parameterization of the JC data.

state contains individual dipolar nanosphere resonances [46, 47]. The spectra are almost identical to the results obtained from standard frequency domain Finite Element Method (FEM) calculations of the absorption spectra for the silver dimer (not shown). The black curves in Figure 2.2(a) are calculated by choosing a fixed value for $\varepsilon_\infty = 8$ and for each frequency ω determining ω_B and $\delta(\omega)$ by equating eqs. (2.7) and (2.8) to the JC data. The red curves are obtained from a random choice of $\varepsilon_\infty(\omega)$ (between 10 and 50) for each frequency and then determiningω_B and $\delta(\omega)$ by equating eqs. (2.7) and (2.8) to the JC data. As expected, both approaches give the same spectra showing that the optical properties of the structure calculated using PH are determined directly by the complex permittivity and independent of the values of the individual parameters ω_B, ε_∞ and δ. In Figure 2.2(b) we compare the resulting real and imaginary refractive indices. As expected, the two different parameterizations give the same results for $n(\omega)$ and $k(\omega)$ and are identical to the JC data. Figure 2.2(c) shows ω_B and $\delta(\omega)$ for the fixed $\varepsilon_\infty = 8$ parameterization.

2.4 Electric field enhancements

We now show how electric field enhancements can be calculated using the PH approach. We pick a small silver nanosphere dimer and include all primitive nanosphere plasmon modes up to an $l_{max} = 20$ to ensure convergence [47, 46].

The PH method expresses the complex potential induced by a dipolar excitation source as the superposition of the potentials generated by each primitive plasmon

mode [19, 47]:

$$\Phi(\vec{r}) = \sum_i \sum_{lm} \frac{1}{2l+1} R_i^2 v_l(r_i, R_i) Y_{lm} \tau_{ilm}(\Omega_i) \tag{2.9}$$

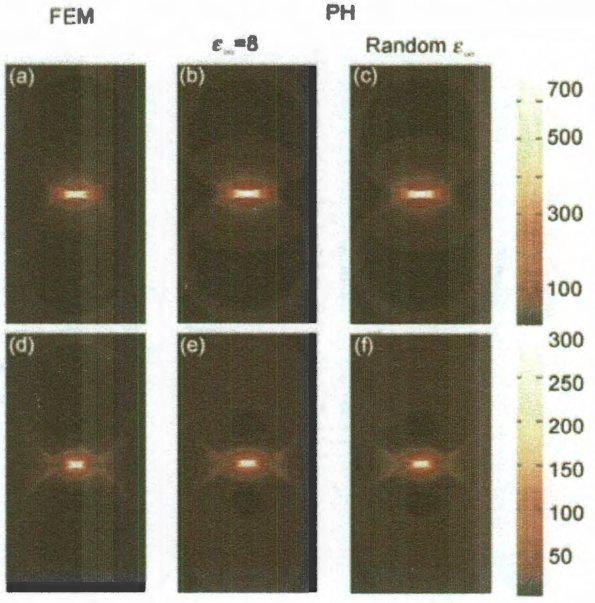

Figure 2.3 : Electric field enhancements for the hybridized dipolar (upper panels) and quadrupolar (lower panels) Ag silver sphere dimer modes calculated using: FEM (a) and (d); PH with the fixed $\varepsilon_\infty = 8$ parameterization of JC data (b) and (e); and PH using the random parameterization of the JC data (c) and (f).

In this expression i is the particle index, R_i is the radius of particle i, r_i is the distance from $\vec{r}$ to the center of nanoparticle i, $Y_{lm}(\Omega_i)$ is the spherical harmonics centered on nanoparticle i. The quantity $v_l(x_1,x_2) = x_<^l / x_>^{l+1}$, where $x_>$ means the larger one of x_1 and x_2 and vice versa for $x_<$. The complex electric field is obtained as the gradient of the complex potential:

$$\vec{E}(\vec{r}) = \nabla\Phi = \sum_{j=x,y,z} (Re[E_j(\vec{r}) + iImE_j(\vec{r})])\hat{j} \tag{2.10}$$

where $\hat{j}$ is a unit vector in the j-direction. The amplitude of the complex electric field gives the magnitude of the local electric field:

$$|E| = \sqrt{\sum_{j=x,y,z} |Re[E_j(\vec{r}) + iImE_j(\vec{r})]|^2} \tag{2.11}$$

In Figure 2.3, we compare the local electromagnetic field enhancements for the two dimer resonances in Figure 2.2(a) calculated using JC data and the numerical FEM (COMSOL) approach with the PH result obtained using the two different parameterizations discussed in Figure 2.2. The figure shows that the results are almost identical. The slight discrepancies between the field enhancements (less than 5%) are caused by numerical grid errors in the FEM and the neglect of retardation effects in PH.

2.5 Summaries and conclusions

In this chapter, we have generally introduced plasmon hybridization method and shown that this method can be extended to include realistic permittivities for metals and to calculate the plasmon-induced electromagnetic field enhancements. In the following chapters, we will further show that by using the 'modes' concept and 'hybridize' concept, lots of interesting optical properties of metallic nanostructures can

be explained in a simple and physical way.

Chapter 3

Fano Resonances in Silver Nanoparticle Heptamers

3.1 Introduction

Plasmonic nanostructures are of considerable current interest because of many important applications in chemical sensing and biosensing,[58, 59, 60] subwavelength waveguiding,[61, 62] metamaterial applications,[63, 64, 65] imaging and fluorescence applications,[66, 67, 68] and biotechnology.[69, 70, 71] The unique ability of plasmons to focus incident light into subwavelength volumes near metal surfaces can lead to very intense local fields. The field intensities of such hotspots can reach sufficient levels to enable single molecule Surface Enhanced Raman Scattering (SERS).[72] The largest plasmonic field enhancements are typically occurring in junctions between adjacent nanoparticles. For this reason much experimental and theoretical effort has been devoted to the study of the plasmonic properties of nanoaggregates such as dimers,[73, 74, 75, 76] trimers and quadrumers,[49, 50, 77, 78] and larger structures such as nanoparticle chains and arrays.[79, 80, 81, 82, 83]

The line widths of plasmon resonances play a crucial role in many applications. In SERS applications the maximum obtainable field enhancements generally become larger for narrower resonances. In waveguiding application, the propagation length is typically proportional to the plasmon lifetime. In Localized Surface Plasmon Res-

onance (LSPR) sensing where analytes are detected through their screening-induced shift of the energy of a plasmon resonance, the efficiency of a plasmonic substrate is typically determined by the Figure of Merit (FoM) defined as the shift of the energy of the plasmon resonance per refractive unit of surrounding material divided by the width of the resonance.[84] In LSPR sensing applications it is therefore crucial to employ substrates with narrow plasmon resonances.

The plasmon line width is determined by both intrinsic and radiative damping. The intrinsic damping is proportional to the imaginary part of the dielectric function and depends on both the material and the wavelength. By employing tunable plasmonic nanoparticles such as nanorods or nanoshells, and tuning the plasmon resonance to a wavelength longer than the onset for interband transitions, the intrinsic damping can be reduced. The radiative damping depends on the total dipole moment of the plasmon resonance. The total dipole moment associated with a collective plasmon mode in a multiparticle aggregate depends on the relative phase of the dipolar plasmon modes of the individual particles. If the individual nanoparticle dipoles oscillate in phase, the plasmon mode is superradiant and strongly radiative. In subradiant modes the dipoles oscillate out of phase, resulting in a drastic reduction of the radiative damping. A dramatic example of the effect of radiative damping has been demonstrated in a concentric ring-disk cavity, i.e., a planar disk concentrically aligned within a planar ring.[85] In this system the dipolar modes of the disk and rings interact and form hybridized bonding and antibonding plasmon modes. The

low-energy bonding mode is subradiant and extremely narrow while the antibonding mode is superradiant and appears like a broad continuum.

The interference between subradiant and superradiant plasmon modes can result in narrow Fano resonances in the optical spectrum of a nanostructure.[64, 86, 87, 88] Apart from their fundamental importance, such Fano resonances are also of considerable interest in LSPR sensing application because of the large FoM that can be achieved for narrow resonances. For instance, for a nonconcentric aligned ring-disk cavity,[86] the FoM of the Fano resonance is larger than 8, which is among the largest FoM reported for a standalone nanostructure.

In a recent study of the plasmonic properties of nanoshell arrays it showed that a symmetric Au nanoshell heptamer can exhibit a pronounced Fano resonance in the infrared part of the spectrum.[89] In this chapter we investigate the microscopic mechanism that provides this interference effect by an application to a smaller symmetric Ag nanosphere heptamer. We show that the heptamer geometry with its unique symmetry properties is particularly amenable to exhibit Fano resonances. According to group theory, the irreducible representation of the symmetric heptamer is the sum of the representation for the center particle (CP) and that of the surrounding six particle ring hexamer (HX). Thus two types of dipolar resonances are formed in this structure, hybridized bonding and antibonding linear combinations of the HX and CP modes. The Fano resonance results from the interference of a narrow subradiant bonding mode of E_{1u} symmetry, which overlaps another broad bonding superradiant

mode of the same symmetry. The Fano resonance of the heptamer is found to exhibit a very large LSPR sensitivity with a FoM above 10.

3.2 Plasmonic Structure of a Heptamer

A number of theoretical methods have been developed for the calculation of the optical properties of nanostructures.[90, 35, 91] In this paper we will use the Finite-Difference Time-Domain method (FDTD),[92] a commercial implementation COMSOL of the Finite Element Method (FEM), and the Plasmon Hybridization (PH) approach.[19] The PH method is an electrostatic approach that expresses the plasmon resonances of a composite nanostructure in terms of the plasmonic modes of the individual constituent nanoparticles. In the present calculation, we include all primitive nanosphere plasmons up to an $l_{max} = 20.$ which is sufficient for convergence.

The metallic particles in this section are assumed to be silver spheres. Normally the Ag metal will be modeled by using experimental dielectric data (JC).[57] To make it easier to resolve individual plasmon modes in the spectra in some instances we will also employ a Drude Fit (DF) where the dielectric function is parametrized as,

$$\varepsilon_{DF} = \varepsilon_{\infty} - \frac{\omega_B^2}{\omega(\omega + i\delta)} \tag{3.1}$$

with $\omega_B = 9.1721eV$, $\varepsilon_{\infty} = 4.039$, and $\delta = 0.0207eV$. This parametrization provides a reasonable fit of the JC data for wavelengths larger than 400 nm. In the electrostatic limit (PH), this parametrization corresponds to sphere multipolar

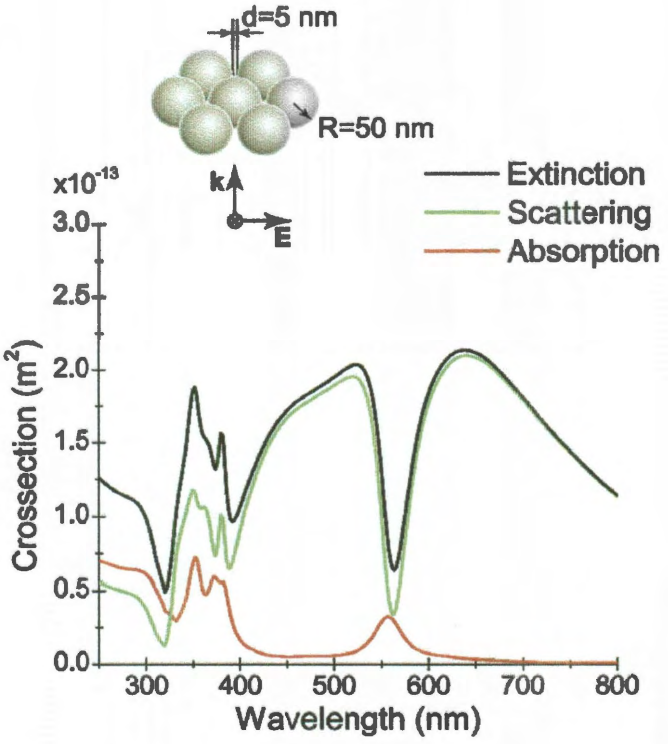

Figure 3.1 : Extinction (black), scattering (green), and absorption (red) cross sections of a symmetric (50,5) nm Ag heptamer calculated for normal incidence, using JC dielectric data.

plasmon energies

$$\omega_l = \omega_B \sqrt{\frac{l}{(\varepsilon_\infty + 1)l + 1}} \tag{3.2}$$

To describe the geometry of a symmetric heptamer consisting of spherical particles of radius R and nearest neighbor separation d we introduce the notation (R, d). All spectra will be calculated assuming normal incidence. As for a symmetric trimer and quadrumer,[49] one can use group theory to show that the symmetric heptamer spectra is independent of the in-plane polarization angle.

In Figure 3.1 we show the different cross sections of a symmetric (50,5) nm heptamer. The extinction and scattering spectra reveal several narrow features. Unless defined explicitly scattering means the electromagnetic energy scattered by a structure from the incident beam integrated over 4π solid angle. The most prominent resonance is the Fano antiresonance around 570 nm. This feature is robust and appears for symmetric heptamers of $R = 50$ nm Ag spheres for interparticle spacings d in the range 2 to 10 nm and probably beyond. The antiresonance at 570 nm is analogous to the Fano resonance discussed for a much larger symmetric nanoshell heptamer.[89]

3.2.1 Plasmon Modes of the Heptamer

In Figure 3.2 we show the plasmon resonances of the heptamer as a function of interparticle spacing calculated using the PH approach. For the largest separation,

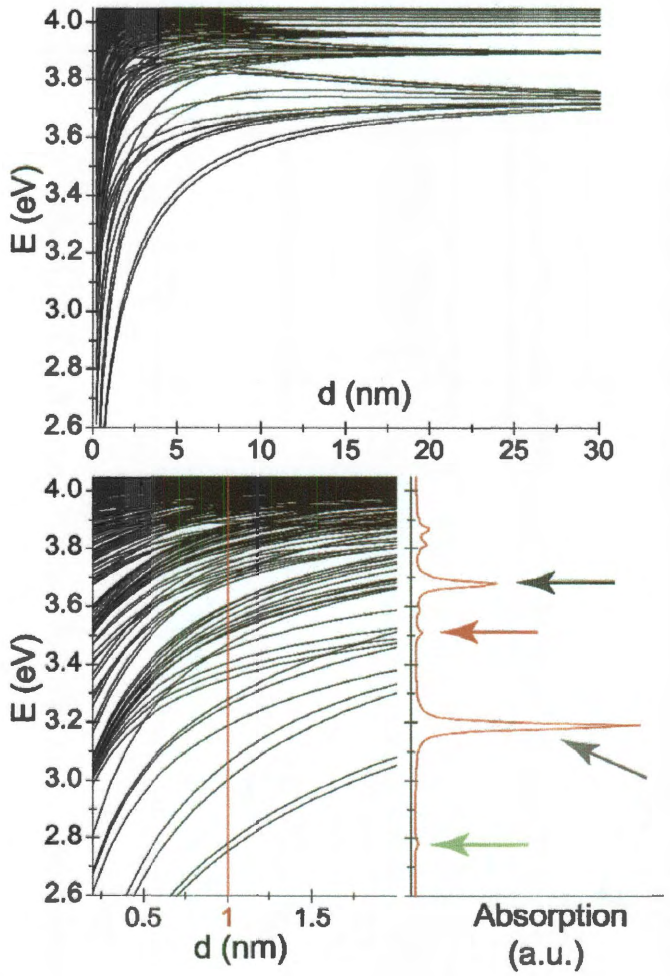

Figure 3.2 : Energy (upper and lower left panels) of the plasmon resonances in a $(10, d)$ nm symmetric silver heptamer calculated as a function of d. The bottom right panel shows the absorption spectra for the $d = 1$ nm structure. The arrows denote some of the dipole active modes. The silver metal is modeled by using the DF parametrization. Only plasmon resonances in the energy interval 2.6 to 4.1 eV are shown.

the interaction between the plasmon modes of different nanoparticles is very small and the plasmon modes are essentially the $7(2l+1)$ degenerate modes of the individual nanosphere plasmon ω_l. As the separation d is decreased, the modes begin to interact and hybridized collective heptamer plasmon modes are formed. The lowest group of levels are the bonding and antibonding modes that asymptotically originate from the dipolar modes. At slightly larger energies, the highly degenerate quadrupolar mode forms a less dispersive manifold of hybridized plasmon modes. Quadrupolar and the higher multipolar resonance interacts very weakly. As the separation is further decreased also modes of different multipolar index l begin to interact resulting in asymmetric splittings of the bonding and antibonding levels. This interaction also results in higher modes becoming dipole active and being able to couple to incident light. This is apparent in the absorption spectrum for $d = 10$ nm, which shows two strong features at 3.5 and 3.7 eV which originate from the $l = 1$ nanosphere modes but also several weak features originating from hybridized $l = 2$ modes.

3.2.2 Group Theory Analysis

The PH approach allows for a very simple interpretation of the plasmonic structure using group theory.[49, 50] The present application to the heptamer closely parallels the previously published application to symmetric trimers and quadrumers.[49]

The heptamer geometry belongs to the D_{6h} point group, and contains two distinct particle types with respect to the symmetry operations. The CP is located at the

intersection of all symmetry elements and it is independent from the six peripheral particles that are connected to each other with group symmetry operators. The heptamer symmetry-adapted basis set is thus the union of that for the HX and that for an isolated sphere. The irreducible representation of the heptamer can thus be written as $\Gamma_{Sept} = \Gamma_{CP} + \Gamma_{HX}$, where the irreducible representations for the planar dipole modes of the sphere and the HX are,

$$\Gamma_{CP} = 2E_{1u}$$

$$\Gamma_{HX} = A_{1g} + A_{2g} + B_{1u} + B_{2u} + 4E_{2g} + 4E_{1u}$$

This decoupling of the symmetry adapted basis for the heptamer into a symmetry adapted basis for the HX and the CP is responsible for the unique plasmonic properties of the heptamer.

For the heptamer there are 21 individual dipolar plasmon modes. We will consider only in-plane modes and assume that the incident E-field is always in the plane of our structure. The 14 individual in-plane dipolar modes transform into 14 symmetry adapted basis functions as illustrated in Figure 3.3. In a dipole representation the CP contributes only to the E_{1u} representation. The E_{1u} representation exhibits a 6-fold degeneracy and the physical plasmon modes are constructed as linear combinations of all 6 E_{1u} basis modes. The CP dipolar plasmon can thus hybridize with the

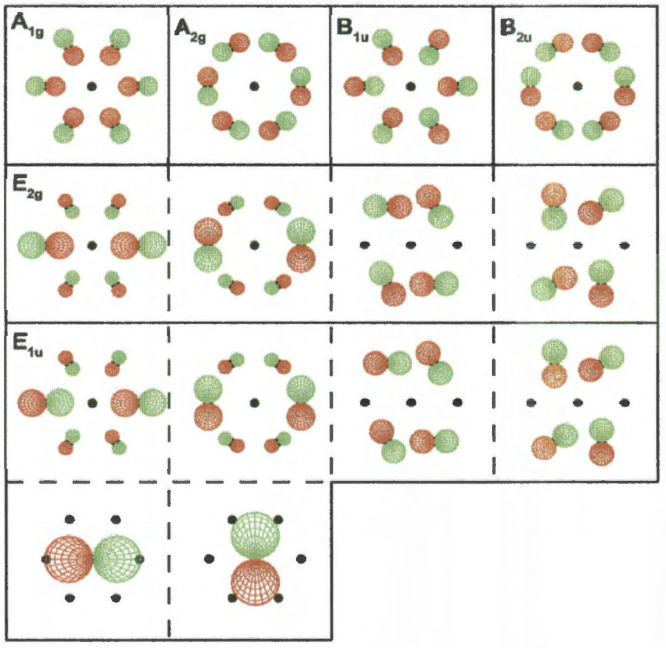

Figure 3.3 : Symmetry adapted basis functions of heptamer planar dipoles generated by using the D_{6h} point group. Only the E_{1u} panels contain modes with finite dipole moments.

surrounding ring dipolar modes and form bonding and antibonding modes as well as dark subradiant and bright superradiant modes.

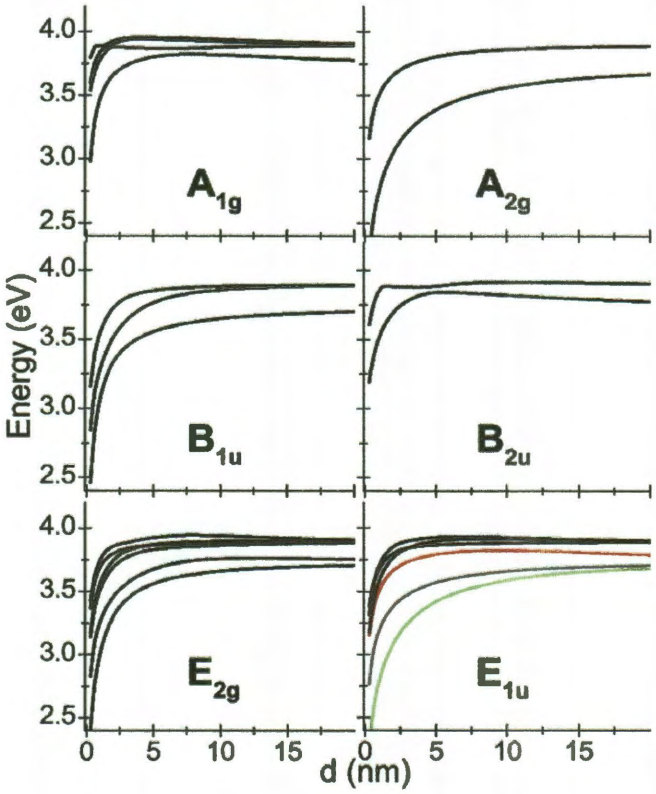

Figure 3.4 : Symmetry resolved plasmon frequencies of the $(10, d)$ nm heptamer as a function of d calculated with PH. The silver metal is modeled by using the DF parametrization. The colored curves of E_{1u} correspond to the features in the absorption spectrum in Figure 3.2.

With use of the symmetry adapted basis function (Figure 3.3), the individual heptamer plasmon modes in Figure 3.2 can be classified by irreducible representation. In Figure 3.4, we show the lowest plasmon modes within each symmetry group as a function of interparticle separation d. The figure shows that for decreasing d the plasmon energies at Figure 3.4 decrease. This red-shift is a specific effect observed

for the heptamer geometry and not observed in smaller systems such as the dimer, trimer, or quadrumer. For example, the dipole modes of A_{1g} symmetry depicted in Figure 3.3 suggest a strong electrostatic repulsion that results in these modes being antibonding in a HX structure. However, in the heptamer this repulsion is countered by an attractive interaction mediated by multipolar plasmons of the CP, which results in an effective attractive interaction and red-shift at small d. Another effect specific to the heptamer geometry is the avoided crossings of plasmon modes, which emerges as a result of the interaction between the CP and the peripheral particles. This effect is responsible for the energy overlap of the subradiant and superradiant modes. The coloring of the E_{1u} modes in Figure 3.4 corresponds to the color of the arrows denoting the peaks in the absorption spectrum in Figure 3.2.

3.3 Analysis of the heptamer Fano Resonance

In this section, we analyze the microscopic origin of the Fano resonance in the extinction spectrum (Figure 3.1) for the (50,5) nm heptamer.

Fano resonances in plasmonic systems can be intuitively understood by using a coupled damped harmonic oscillator model originally developed as a classical analogy to Electromagnetically Induced Transparency (EIT) in atomic systems.[93] Fano resonances appear naturally in such systems when narrow dark modes couple to and spectrally overlap broad bright modes. The effective interaction between the two such modes is dispersive and can result in a strong interference in the oscillator amplitudes

which in turn influence the radiation emitted from the system, i.e. the scattering spectrum. When the two oscillator modes are of similar frequency the interference results in a symmetric antiresonance. If the frequencies are different, the typical asymmetric Fano resonance appears. The PH method directly expresses plasmons in composite nanoparticles as coupled damped harmonic oscillators. Dark plasmons with little or no dipole moments are narrow, and bright plasmons with sizable dipole moments are superradiant and strongly damped. The interaction between plasmon modes on adjacent nanoparticles is controlled by the geometry of the structure.

In Figure 3.5 we show the scattering and absorption spectra for the heptamer with all dimensions scaled down by a common factor. For the smallest system $(10, 1)$ nm, the scattering and radiative damping is very small and the absorption spectrum agrees perfectly with the result from the electrostatic PH approach shown in Figure 3.2. The two strong features at 340 and 380 nm are the two bonding E_{1u} modes (black and blue lines in Figure 3.4). The very weak feature at 450 nm is the almost dark bonding subradiant E_{1u} (green line in Figure 3.4) with the dipole moment of the center atom oriented opposite to the dipole moment of the surrounding six ring atoms. The nature of this mode will be discussed in detail below.

As the size of the system is increased, scattering becomes more important than absorption. The superradiant E_{1u} mode begins to red-shift and broadens significantly while the dark mode remains narrow and red-shifts only weakly. For $R > 25$ nm, the superradiant mode is sufficiently broad to overlap the dark mode. When this

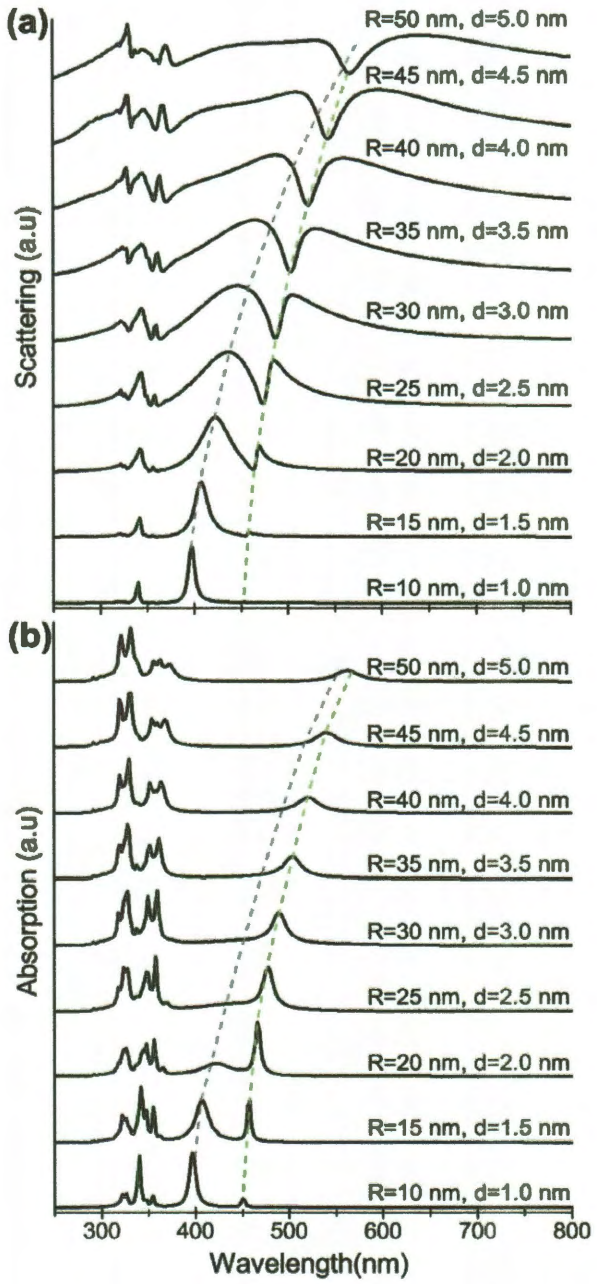

Figure 3.5 : Scattering (a) and absorption (b) spectra calculated with FEM of the heptamer as a function of overall size of the system. The Ag is modeled by using the DF dielectric parametrization. The dashed curves show the red-shift of the subradiant (green) and superradiant (blue) modes with increasing size.

happens, the conditions for radiative plasmonic interference effects are satisfied. The dispersive coupling between the narrow subradiant mode and the broad continuum of the superradiant mode results in an asymmetric Fano resonance at the energy of the subradiant mode. For $R = 50$ nm, the energies of the subradiant and superradiant modes are approximately equal and a characteristic antiresonance appears in the spectra.

The absorption spectra in Figure 3.5b illustrate the dramatic effect radiation damping has on the line width of bright plasmon resonances in finite systems of increasing size. For R larger than 25 nm, the superradiant mode is not discernible in the absorption spectrum. The reason for that is that the mode radiates much more strongly than it absorbs. Although the mode still exhibit a finite albeit small absorption, the intensity is too small to result in a Fano resonance in the absorption spectra.

In Figure 3.6 we show the electric field enhancements of the subradiant and superradiant modes for the $(10, 1)$ nm heptamer calculated using PH. This small heptamer is in the quasistatic regime, so FEM and PH both give the same results. We also show the field enhancements for three wavelengths around the Fano resonance for the $(50, 5)$ nm heptamer where retardation effects play a dominant role. These plots are very similar to the result for the electrostatic $(10, 1)$ nm system where a group theoretical analysis can be rigorously justified. The dipolar components of the modes calculated with PH are shown in Figure 3.6a–c and clearly show that both the

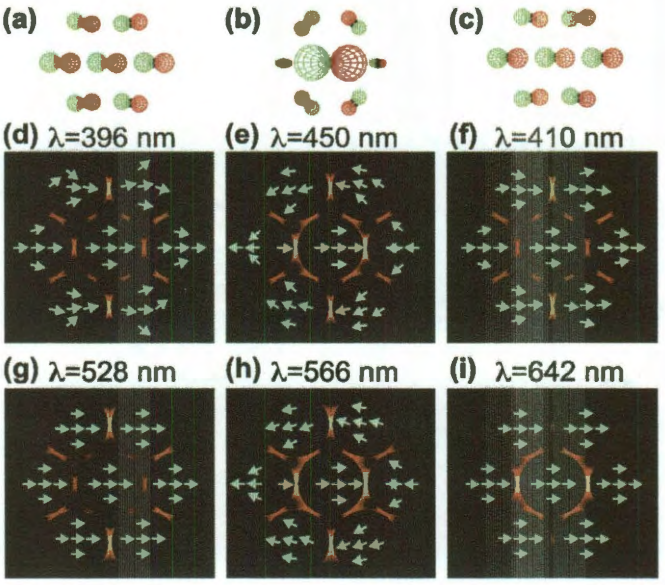

Figure 3.6 : Electric field direction (blue arrows) and enhancement (color contour with red and yellow indicating hot spots) associated with the subradiant (center column) and on the blue (left column) and red (right column) sides of the superradiant heptamer plasmon modes. Panels a—c show the dipolar admixtures calculated with PH. Panels d—f are for the $(10, 1)$ nm heptamer and panels g—i are for the $(50, 5)$ nm heptamer. The maximum field enhancements for the $(50, 5)$ nm heptamer are 53, 88, and 43 at 528, 566, and 642 nm wavelengths.

subradiant and superradiant modes are different bonding linear combinations of the symmetry-adapted basis functions depicted in the E_{1u} panel of Figure 3.6. For the superradiant mode, the dipolar mode of the CP oscillates with the same phase as the dipolar plasmons in the surrounding ring and therefore exhibit significant broadening due to radiation damping. For the subradiant state, the dipole moment of the CP is opposite to the dipole moments of the ring plasmons. Thus the total dipole moment is reduced and the width of the resonance is determined by the intrinsic damping.

Since the symmetry properties of the heptamer are such that the plasmon modes can be regarded as having been formed through hybridization of the modes of the CP and those of the surrounding HX, it is of interest to investigate the effect of changing the radius of the CP. Such a change does not break the symmetry of the heptamer. In Figure 3.7a, we show the extinction spectra of the $(50, 5)$ nm heptamer when substituting the CP with a sphere of different radius RC. For the smallest $RC = 20$ nm, the interaction between the CP and the surrounding HX is negligible and the spectrum is essentially a superposition of the spectra for a $(50, 5)$ nm HX and the spectrum of a silver nanosphere of radius 20 nm. The plasmonic structure of the HX will be analyzed in detail elsewhere. Briefly, the optically active modes are linear combinations of the first four basis functions of E_{1u} symmetry depicted in Figure 3.3. The HX modes that are relevant in the present discussion include a relatively narrow mode around 400 nm and a continuum extending between 425 and 800 nm that is made up of two superradiant modes centered around 450 and 600 nm. The 400 nm

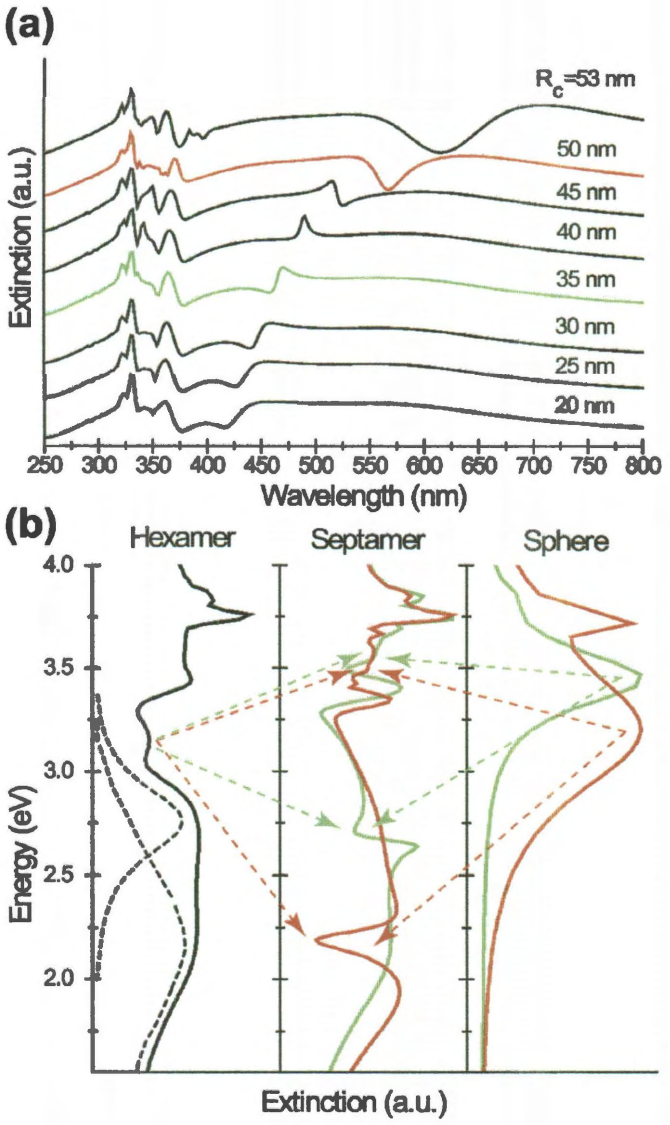

Figure 3.7 : (a) Effect of replacing the CP in a $(50, 5)$ nm heptamer by a sphere of different radius $RC = 35$ nm (red) and 50 nm (green). (b) A PH hybridization diagram showing how the bonding subradiant heptamer mode (center) is formed from the interaction of the HX (left) and the CP (right). The two dashed lines in the HX are two different and overlapping superradiant HX states. The arrows represent the interactions between the relevant states.

mode interacts with the CP dipole to form the hybridized bonding subradiant mode depicted in Figure 3.6b. This mode is highly tunable with a wavelength that depends strongly on RC. As the radius RC becomes larger, the interaction between the CP plasmons and ring plasmons increases and interference effects begin to play a role. For $RC = 35$ nm, the subradiant mode begins to interfere with the short wavelength edge of the HX continuum resulting in a characteristic asymmetric Fano resonance at 450 nm. As RC increases, the interaction increases resulting in a further red-shift of the subradiant state into the HX continuum and a change of the line shape of the Fano resonance. For the largest $RC = 50$ and 53 nm, the Fano resonance appears as an antiresonance in the lower energy HX continuum.

In Figure 3.7b we illustrate schematically how the plasmon resonances of the CP and the surrounding HX hybridize to form the subradiant state that results in the Fano resonance. To make the PH more apparent the extinction spectra are plotted as a function of energy rather than wavelength. The figure clearly shows how the dipolar nanosphere plasmon interacts with a HX mode around 3.2 eV and forms a bonding subradiant mode in the HX continuum. For $RC = 35$ nm, the subradiant state is red-shifted to around 2.7 eV, where it appears as an asymmetric Fano resonance. For $RC = 50$ nm, the state is further red-shifted to 2.2 eV and appears in the spectrum as an antiresonance.

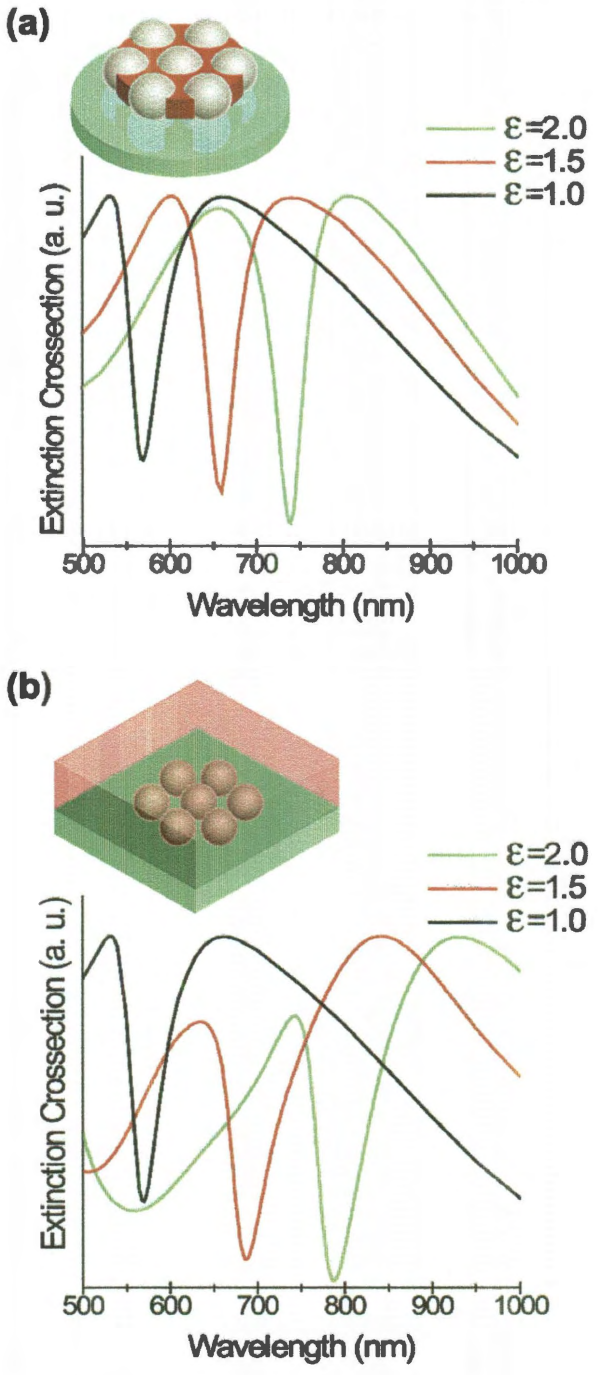

Figure 3.8 : Effect of partially (a) and completely (b) surrounding a $(50, 5)$ nm heptamer by dielectric media on the extinction spectrum. The permittivities are 1.0 (black), 1.5 (red), and 2.0 (green). The heptamer is placed on a glass substrate of permittivity 2.09. The metal is modeled by using JC. The shape of the dielectric insertions is indicated in the insets.

3.4 LSPR Sensing

Plasmonic interference and coherence effects such as Fano resonances are caused by plasmon–plasmon interactions and can therefore be very strongly affected by the electrostatic screening introduced by the presence of dielectric media between adjacent nanoparticles.[86] The heptamer Fano resonance with its distinct and narrow shape in the visible region of the spectrum thus provides an interesting candidate as an efficient LSPR sensor. In Figure 3.8 we show the extinction spectra of a heptamer placed on a glass substrate surrounded by dielectric embedding media of different permittivities. Figure 3.8a shows the effect of only filling the junctions with the embedding media and Figure 3.8b shows the effect of completely covering the heptamer structure. Both panels demonstrate that the effect of dielectric screening is a strong red-shift of the Fano resonance. The LSPR shift for the Fano resonance in Figure 3.8a is 410 nm/RIU and for a complete embedding of the heptamer as shown in Figure 3.8b, the LSPR shift is 515 nm/RIU. The full width half-maximum of the Fano resonance defined as the energy difference between the peak on the short wavelength side of the antiresonance and the energy of its minimum is 0.15 eV. The corresponding FoM are thus 7.9 and 10.6, which shows that the heptamer structure would provide an excellent platform for LSPR sensing.

The plasmonic interference effects responsible for the large LSPR sensitivity originate from the particular symmetry properties of a heptamer and are likely to arise also for heptamers consisting of cylindrical disks which may be readily fabricated by

using lithographic techniques.

3.5 Summaries and conclusions

In this chapter, using numerical and analytical electromagnetic methods we have analyzed the optical and plasmonic properties of symmetric Ag nanosphere heptamers. The unique symmetry of a heptamer leads to a decoupling of its plasmon modes into plasmon modes of the six surrounding ring particles and the plasmon modes of the center particle. The interaction between the plasmon modes of the center particle with the plasmon modes of the surrounding ring results in hybridized bonding and antibonding heptamer plasmon. The interference between a bonding subradiant and a bonding superradiant heptamer plasmon results in a pronounced Fano resonance in the extinction spectrum. This Fano resonance is found to be well preserved also for a weak structural symmetry breaking of the heptamer. The Fano resonance is found to exhibit an unusually large LSPR sensitivity making the heptamer structure a highly promising substrate for LSPR sensing.

Chapter 4

Fano resonances in planar nanosphere clusters

4.1 Introduction

The Localized Surface Plasmon Resonance (LSPR) in nanostructures is a subject of intensive current interest, because of many promising applications in both biological and physical sciences [94, 95, 96, 97]. Many of these applications are based on the large electromagnetic field enhancements of "hot-spots" that can be induced for resonant excitation of their plasmon resonances. These field enhancements [98, 99] amplify the cross sections for Surface Enhanced Raman Scattering (SERS) [100, 101, 102] or Surface Enhanced Infrared Absorption (SEIRA) [58, 89, 103, 104].

The plasmon resonances of a nanoparticle strongly depend on its geometry and composition [104, 105, 106, 107]. Examples of tunable nanostructures capable of providing large electromagnetic field enhancement are nanoparticle pairs or "dimers". In these structures, the electromagnetic coupling between the plasmon resonances of the individual nanoparticles results in hybridized plasmon modes that provide intense hot-spots in the gaps between the particles [108, 109, 110, 111, 112].

Recently much attention has been devoted to nanoparticle aggregates consisting of more than two nanoparticles, such as trimers [113, 78, 114, 115, 49], tetramers [116, 117, 118], as well as ordered or disordered nanoparticle arrays [119, 81, 120, 121,

122]. In addition to providing an enhanced plasmonic tunability relative to the dimer system, larger nanoparticle aggregates support larger electric field hot-spot volumes. Larger structures such as symmetric heptamers are also of significant interest in LSPR sensing applications because their plasmon modes exhibit radiative interference effects resulting in very narrow Fano resonances with unusually high spectral sensitivities to the dielectric environment of the nanostructure [89, 51, 123].

In this chapter, we first present an investigation of the plasmonic structure of several different silver nanoparticle aggregates. We show that group theory can be used to interpret the plasmon resonances in highly symmetric clusters. For clusters consisting of large spheres, where radiative effects become more important, we show that sharp Fano resonances appear in the optical spectra. We also present a more detailed investigation of the Fano resonances in the symmetric heptamer cluster and other related particle in ring (PIR) structures. In the end, as experimental examples, we present two interesting structures: gold heptamers and gold quadrumers. These nanostructures are made by self-assemble technic. We also analyze the characters of Fano resonances of these two structures.

4.2 Plasmon resonances in small sphere clusters

To calculate the optical properties of nanoparticle clusters, we use the COMSOL implementation of the Finite Element Method (FEM) and the Plasmon Hybridization (PH) method. For both approaches we model the silver nanoparticles using the

Johnson & Cristy (JC) experimental dielectric data [57]. The PH method is an exact electrostatic approach which expresses the plasmon resonances of a system of interacting nanoparticles as hybridized linear combinations of the "primitive" plasmon modes of the individual particles [124]. Mathematically, the PH method is equivalent to molecular orbital theory where the molecular orbitals are expanded in linear combinations of atomic orbitals. Although the PH approach neglects phase retardation effects, it provides a simple and intuitive understanding of the microscopic nature of the plasmon modes in complex plasmonic nanostructures and has established a paradigm of plasmonic nanostructures as a type of artificial molecule [124].

In the present problem, the individual nanoparticles are assumed to be solid silver spheres. The primitive plasmon resonances are thus the multipolar plasmon modes of all the individual nanospheres in the cluster. As in any coupled system, the effective hybridization of two modes depends on the ratio of the mode-mode interaction strength and the energy difference between the two modes. For large interparticle spacings where the mode-mode interaction is weak, the hybridized nanoparticle cluster plasmon modes will essentially only contain primitive plasmons of the same multipolar index. However, for small interparticle separations where the interaction between primitive plasmons of different multipolar order can be large, primitive plasmon modes of different multipolar order will also mix. For such structures, the hybridized modes will contain primitive plasmon modes of all multipolar orders. For simplicity we will refer to such hybridized plasmon modes by using the multipolar

order to which they would correspond in the limit of large separation.

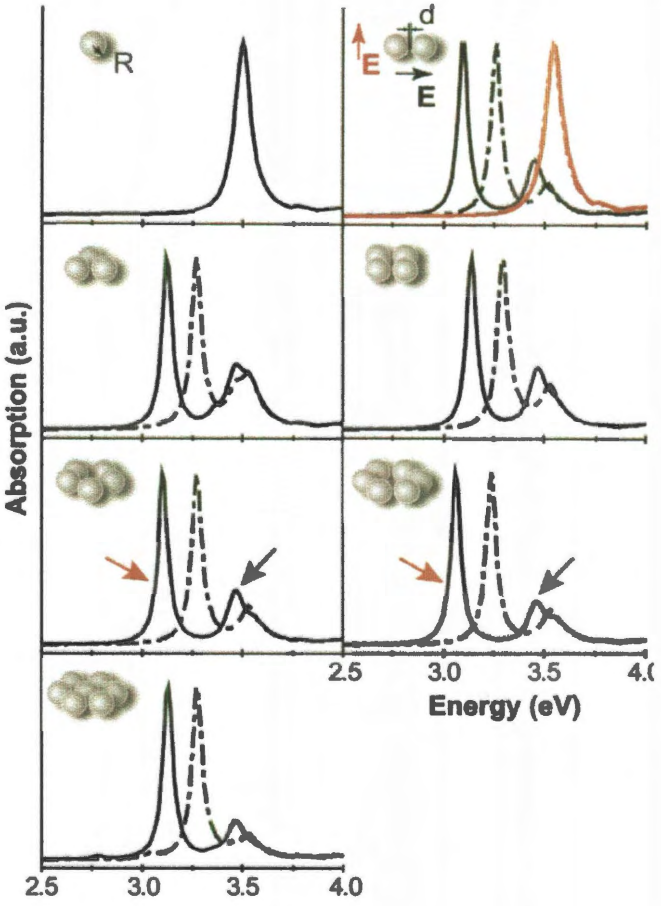

Figure 4.1 : Absorption spectra for small silver sphere clusters (monomer, dimer, trimer, quadrumer, pentamer, hexamer and heptamer) calculated using PH. The radii of the spheres are assumed $R = 10$ nm and the interparticle distance$d = 2$ nm (dashed) and $d = 1$ nm (solid). The particle configuration and the incident field direction is depicted in the insets. The silver metal is modeled using JC data

In Fig. 4.1, we show the calculated optical absorption for in-plane polarization of symmetric clusters consisting of $N = 1$–7 (monomer, dimer, trimer, quadrumer, pentamer, hexamer and heptamer) small silver nanospheres of radii $R = 10$ nm and interparticle separations $d = 1$–2 nm. The monomer spectrum exhibits a single po-

larization invariant absorption peak corresponding to its dipolar plasmon resonance. The dimer spectrum is polarization dependent. For longitudinal polarization, two peaks appear corresponding to the bonding dipolar and quadrupolar dimer plasmon. The hybridized quadrupolar dimer plasmon is visible because of the admixture of primitive dipolar plasmons in its state function. The dimer spectrum for transverse polarization is very similar to the monomer spectra and shows only a weak dependence on nanoparticle separation. For larger ($N \geq 3$) clusters, one can prove rigorously that the spectra are independent of the polarization direction because the dipolar modes belong to a degenerate two-dimensional representation [49]. For trimer and larger clusters the spectra exhibit two or more hybridized plasmon resonances (dipolar and higher multipolar) that redshift with decreasing nanoparticle separation.

Figure 4.1 also shows that the absorption spectra are remarkably insensitive to the detailed structure of the cluster. The reason for this is because the plasmonic interactions are short range and the plasmon modes are determined by the nearest neighbor interactions. However, as will be shown in section 3, for clusters consisting of larger nanoparticles where scattering and longer range radiative effects become dominant, the spectra for various cluster arrangements can be significantly different.

Due to the weak plasmonic interactions for transverse polarization, the spectra for light polarized perpendicularly to the clusters show only a single absorption peak (not shown). We therefore focus our attention on the spectra obtained for in-plane polarization.

In some other publications group theory has been used to analyze the plasmonic properties of trimers and quadrumers [49], and the heptamer [89, 51]. In the next subsection, we perform a similar analysis for the pentamer ($N = 5$) and the hexamer ($N = 6$).

4.2.1 A Group theoretical analysis for the plasmon modes of the pentamer and hexamer

The pentamer belongs to the D_{5h} symmetry group and its reducible planar dipolar representation contains 10 individual particle dipoles that correspond to the following irreducible representations,

$$\Gamma_{PT} = A_1^{'} + A_2^{'} + 4E_1^{'} + 4E_2^{'} \tag{4.1}$$

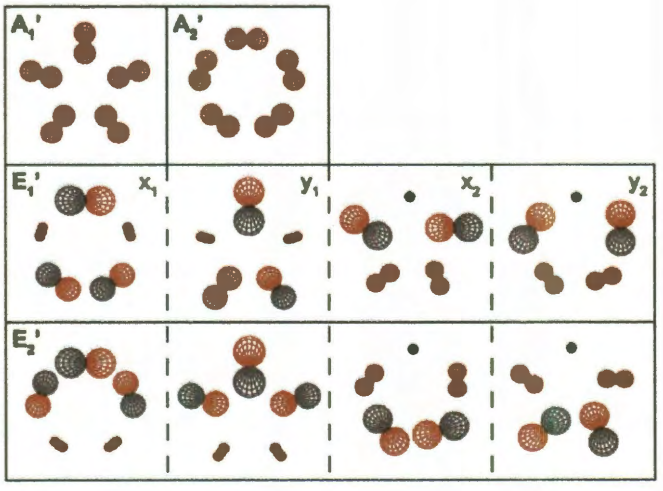

Figure 4.2 : Symmetry-adapted planar dipolar modes of a symmetric pentamer. Modes with non-zero dipole moment are labeled as x_1, x_2, y_1, y_2 indicating the predominant directions of the dipoles

The symmetry-adapted planar dipolar modes for the pentamer, for each irreducible representation, is shown in Fig. 4.2. Only the four E_1 modes have non-zero dipole moments and may couple to light in the dipolar limit. These four modes combine and form two doubly degenerate states, two bright bonding modes with large dipole moments and two dark antibonding modes with negligible dipole moments. The degeneracy of each state corresponds to the direction of the in-plane dipole components.

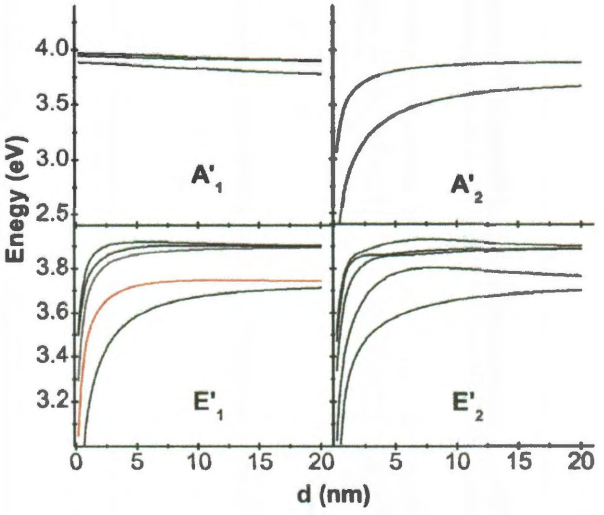

Figure 4.3 : Symmetry resolved dipolar pentamer plasmon modes as functions of the interparticle separation. The red and blue lines are the modes indicated in Fig. 4.1

The pentamer plasmon modes can be classified according to their irreducible representation. In Fig. 4.3 we show the lowest energy dipolar and quadrupolar modes of each symmetry as a function of interparticle separation d. The red and blue curves in the E_1 panel are the hybridized dipolar and quadrupolar pentamer modes responsible for the two absorption resonances indicated in Fig. 4.1. For large separations,

the plasmon modes approach the individual sphere dipolar and quadrupolar plasmon modes. When the particles are closer and interact more strongly, those modes show varying behavior according to the symmetry of the plasmon surface charges. The A_1 modes are antibonding as predicted by the group theory analysis in Fig. 4.2 and their energies increase for smaller interparticle distance d. The other modes are bonding modes with energies that decrease with d.

The hexamer belongs to the D_{6h} symmetry group and its reducible planar dipolar representation contains 12 individual particle dipoles that correspond to the following irreducible representations,

$$\Gamma_{HX} = A_{1g} + A_{2g} + B_{1u} + B_{2u} + 4E_{2g} + 4E_{1u} \tag{4.2}$$

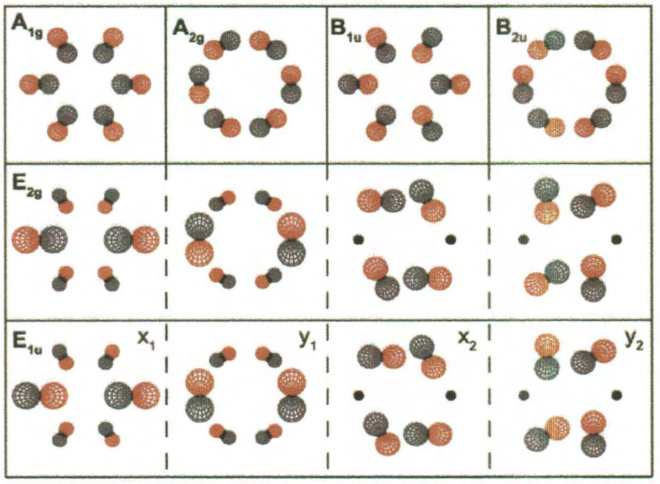

Figure 4.4 : Symmetry-adapted planar dipolar modes of a symmetric hexamer. Modes with non-zero dipole moment are labeled as x_1, x_2, y_1, y_2 indicating the predominant directions of the dipoles

The symmetry-adapted planar dipolar modes of the hexamer for each represen-

tation is shown in Fig. 4.4. Only the four E_{1u} modes have non-zero dipole moment and can couple to light in the dipolar limit. As for the pentamer, the degenerate E_{1u} modes combine to form two degenerate pairs of bright and dark modes. However, the higher symmetry of the hexamer leads to a stronger hybridization with higher multipolar modes.

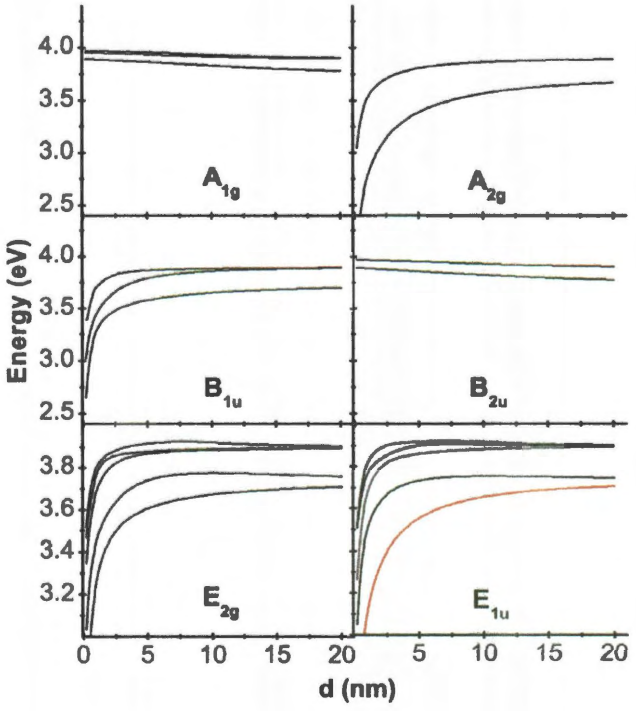

Figure 4.5 : Symmetry resolved planar dipolar hexamer plasmon modes as functions of the interparticle separation. The red and blue lines are the modes indicated in Fig. 4.1

In Fig. 4.5 we show the lowest energy dipolar and quadrupolar hexamer plasmon modes of each symmetry as a function of d. The red and blue curves in the E_{1u} panel are the hybridized dipolar and quadrupolar hexamer modes responsible for the two absorption resonances in Fig. 4.1. The A_{1g} and B_{2u} modes of a hexamer are

antibonding and their energies increase with decreasing interparticle separation d. The other modes are bonding with energies that decrease with d.

4.2.2 Surface charge distributions in the pentamer and the hexamer modes

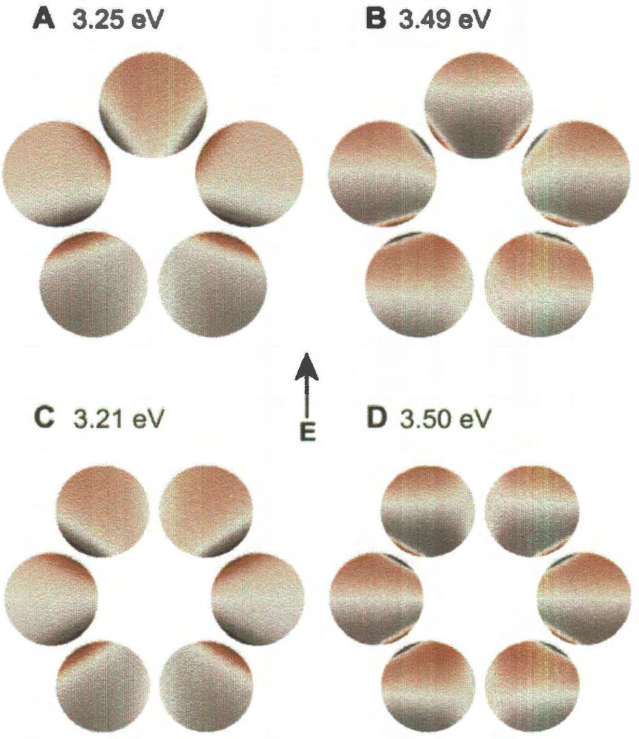

Figure 4.6 : Top view of the induced surface charge from negative (blue) through zero (white) to positive (red) for the absorption maxima in the pentamer modes at low energy (A), high energy (B); hexamer modes at low energy (C), high energy (D)

The calculated electric field enhancements for the $N \geq 2$ structures in Fig. 4.1 are localized in the junctions between the nanospheres. For the lowest energy dipolar modes, the field enhancements are larger than 200 and for the quadrupolar resonances of the order 100. In Fig. 4.6 we show the calculated charge distributions associated

with the two lowest energy absorption resonances for the pentamer and the hexamer discussed in Fig. 4.1. Panels 4.6A and 4.6C shows the charge distribution for the lowest energy dipolar modes (red arrows in Fig. 4.1 and red lines in Figs. 4.3 and 4.5). The spatial distribution of the induced charges reveals that the mode is predominantly dipolar but also contains an admixture of quadrupolar modes. Due to the strong interactions between adjacent nanoparticles, the surface charges are confined near the interparticle junctions. This orients the dipoles in a manner that reflects the symmetry of the cluster. The dipolar patterns correspond directly to states that can be obtained by combining the different symmetry-adapted modes for the pentamer from Fig. 4.2 and Fig. 4.4. For instance, the charge distribution in Fig. 4.6A corresponds to the y_1 mode in the E_1 representation in Fig. 4.2 with an addition of x_2 and y_2 modes and higher order components. The charge distribution in Fig. 4.6C is very similar to the y_1 mode in the E_{1u} representation in Fig. 4.4 with slight admixtures of the x_2 and y_2 modes and higher order components.

Panels 4.6B and 4.6D show the charge distribution for the higher-energy quadrupolar modes (blue arrows in Fig. 4.1 and blue lines in Figs. 4.3 and 4.5). The spatial distributions of the induced charges are predominantly quadrupolar but also reveal a dipolar admixture as expected from the hybridization of the primitive plasmon modes. The dipolar admixture in these hybridized quadrupolar modes corresponds to linear combinations of the symmetry-adapted dipolar modes shown in the E_1 panel of Fig. 4.2 for the pentamer and the E_{1u} panel of Fig. 4.4 for the hexamer.

4.3 Optical spectra for large sphere clusters

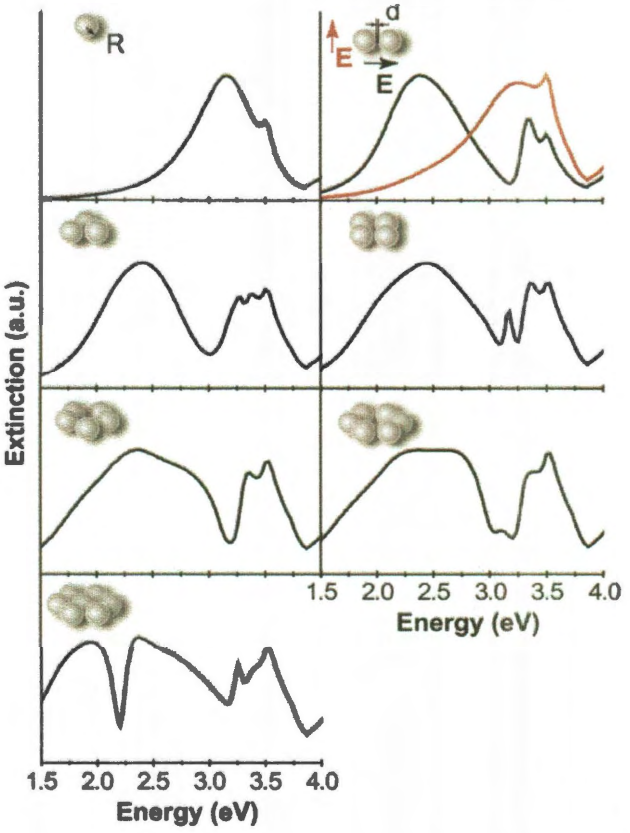

Figure 4.7 : Extinction spectra calculated using FEM for silver nanospheres of $R = 50$ nm and interparticle separation $d = 5$ nm. The silver metal is modeled using JC data

In Fig. 4.7 we show the extinction spectra for the same clusters as in Fig. 4.1 but for $R = 50$ nm and $d = 5$ nm. In the scale invariant electrostatic limit (infinite velocity of light), the spectra of these larger structures would have been identical to those for $d = 1$ nm in Fig. 4.1. The large differences between the spectra in Figs. 13 and 19 are thus caused by phase retardation. The major effects of the phase retardation on plasmon modes are dipolar resonance redshifts and broadenings. Another effect is the increased coupling of light to higher multipolar cluster plasmon modes. For

small clusters the coupling to such modes is indirect due to the admixture of dipolar primitive plasmons into the hybridized multipolar modes. For larger structures, the phase variation of the incident electromagnetic wave across the structure enables a direct coupling to higher multipolar order plasmons.

The lowest energy dipolar plasmon resonances in Fig. 4.7 exhibit strong redshifts and broadenings compared to the corresponding curves in Fig. 4.1. For the hybridized quadrupolar modes, the intensities increase and the peaks exhibit smaller redshifts and less broadenings than the dipolar resonances. In addition, new structures and features with distinctly asymmetric line shapes appear in the spectra. These are Fano interference resonances caused by the interaction between broad continuum-like plasmon resonances and narrow sharp discrete plasmon modes [86, 38]. The monomer resonance around 3.4 eV is caused by the interaction of the broad dipolar nanosphere plasmon with the narrow quadrupolar Mie resonance [125, 126]. Large plasmonic clusters exhibit a much richer variety of broad and narrow modes. Broad continuum-like plasmon resonances are provided by superradiant modes, i.e. collective dipolar modes where the individual primitive dipolar plasmons of the constituent particles oscillates in phase resulting in a large total dipole moment and strong radiative damping. Narrow and sharp modes are provided by subradiant modes where the total dipole moment is zero, either due to the individual nanoparticle dipoles oscillating out of phase or because the hybridized modes do not contain substantial admixtures of primitive dipolar components [89].

The pronounced Fano resonance around 2.1 eV for the heptamer structure has been discussed extensively in a previous publication [51] and was recently observed experimentally in an individual nanoshell heptamer [123]. A major requirement for a strong Fano resonance is a significant spectral overlap of the continuum-like and the narrow modes [127]. Due to the particular symmetry of the heptamer cluster, the optically active modes of E_{1u} symmetry are hybridized bonding and antibonding combinations of the center particle and the surrounding ring modes [51]. For the heptamer, the individual dipolemoments of the ring and center particle modes are almost equal. The hybridization thus leads to a bonding subradiant mode with almost no net dipole moment and an antibonding superradiant mode with a large total dipole moment equal to the sum of the center particle and ring dipole moments. Due to phase retardation, the superradiant mode is redshifted to an energy very close to the subradiant mode. The interference thus results in an almost perfect antisymmetric Fano resonance [123].

The symmetric heptamer with its very narrow Fano resonance provides a system with exceptional LSPR sensitivity [51]. It is therefore of an interest to investigate the plasmonic structure of other similar nanoparticle cluster to determine if similarly strong Fano resonances can appear. In the next section we present an extensive investigation of the optical properties of several other particle-in-a-ring structures (PIR).

4.4 Fano resonances in large PIR clusters

In Fig. 4.8 we show the extinction spectra for several different PIR clusters. The left column shows structures where all particle have the same radii. For the three smallest clusters (N = 4–6), the interparticle spacings in the surrounding ring are too large for strongly interacting ring modes to develop. In these small clusters, the plasmonic interactions occur primarily between the center particle and the nearest ring particle. The spectra therefore look qualitatively similar to the longitudinally polarized dimer spectrum in Fig. 4.7. The smallest strongly interacting PIR structure consisting of particles with equal radius is the heptamer discussed in Fig. 4.7. For the $N = 8$ and $N = 9$ clusters in the left column of Fig. 4.8, a Fano resonance appears around 2.3 eV. The physical origin of this resonance is the same as for the heptamer, i.e., interference between a bonding dark and antibonding bright collective mode. However, since the ring dipole moments for these structures are larger than for the heptamer, both hybridized modes possess finite dipole moments and can couple directly to incident light. A direct coupling of incident light to the dark mode alters the Fano interference conditions and can result in a drastic change of the line shape of the Fano resonance [86]. For the larger $N = 9$ and $N = 11$ clusters in the left column of Fig. 4.8, the spacing between the center particle and the ring is too large to result in significant coupling.

In the right panel of Fig. 4.8, the radius of the center particle is adjusted to maintain a small and constant interparticle separation and thus ensure strong couplings

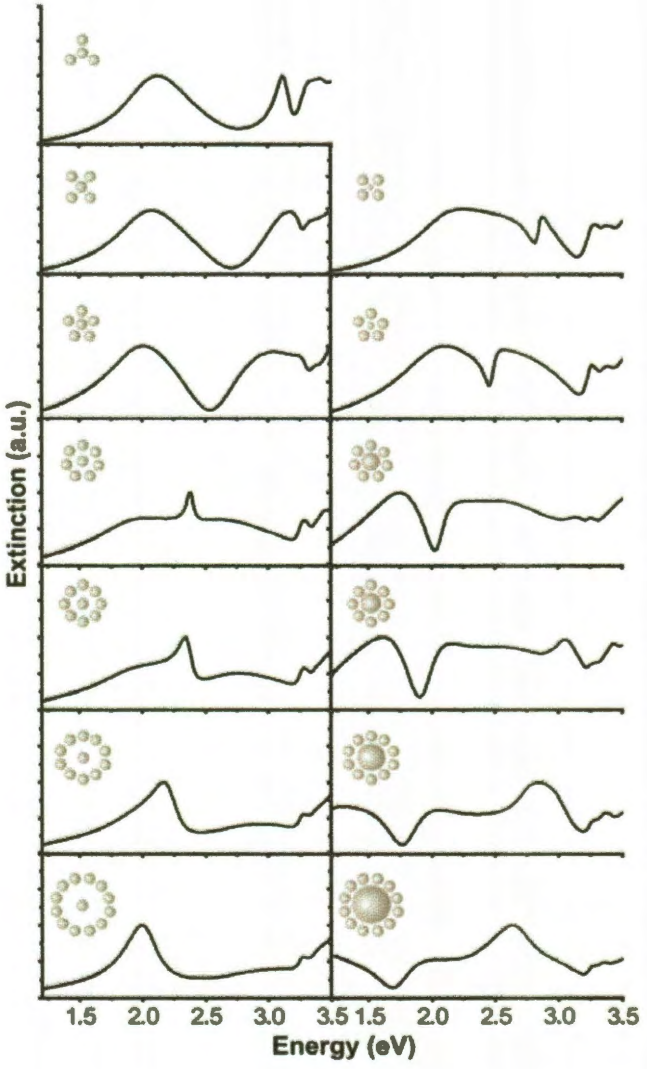

Figure 4.8 : Extinction spectra of symmetric silver nanoparticle clusters calculated using FEM. (Left) All particles have R = 50 nm and the smallest interparticle spacings are 5 nm. (Right) For peripheral particles R = 50 nm. The radius of the center particle is varied so that all interparticle spacings are 5 nm. The dielectric data for the silver metal is modeled using JC

between all particles. It is interesting to note that both the $N = 6$, $N = 8$ and $N = 9$ clusters exhibit sharp and well-defined Fano resonances with lineshapes characteristic of subradiant modes. The reason why the antibonding modes remain dark for different ring sizes is that the radius of the center particle and thus its dipole moment is varied. What made the heptamer unique was the almost perfect cancelation of the ring and center particle dipole moments in the bonding dark mode. This cancellation occurred because the dipole moments of a six-membered ring and the center particle were equal [51]. For the $N = 6$, $N = 8$ and $N = 9$ clusters the ring dipole moments remain similar to the center particle dipole moments leading to efficient cancellation of the dipole moment of the bonding dark mode. However, although several of the clusters in Fig. 4.8 exhibit sharp Fano resonances, none is as sharp as the Fano resonance for the symmetric heptamer shown in Fig. 4.7.

4.5 Two experimental examples: Fano resonances in gold heptamers and quadrumers

4.5.1 Gold heptamers

Traditionally, plasmonic nanostructures are fabricated on planar substrates by top-down processes such as electron-beam lithography or focused–ion beam milling. With these methods, geometries as varied as split rings and coupled nanorods can be patterned with precise substrate positioning, leading to structures that support electric, magnetic [128, 129], and Fano-like resonances [130, 127]. Fano-like resonances arise

from interactions between a superradiant "bright" mode and a subradiant "dark" mode in a nanostructure, and they are characterized by a pronounced minimum in the scattering spectra. These fabrication routes have several fundamental limitations. First, the spatial resolution of the structures is limited to ~10 nm by the electron- and ion-beam size and the metal grain size. Second, these routes produce planar thin-film architectures that are generally unsuitable for complex three-dimensional (3D) fabrication. Third, there is limited optical coupling between thin-film nanostructures defined within the same plane. Stronger coupling can be attained by vertically stacking plasmonic structures [128, 127], but this fabrication strategy is challenging.

The self-assembly of metallic colloids [131, 132] provides a versatile and low-cost route to the construction of complex 2D and 3D optical materials. We show that self-assembled clusters of spherical metal-dielectric colloids have optical properties that can be controlled by varying the number and position of particles in the cluster. As such, a hierarchy of tunable plasmonic structures that exhibit strong electric, magnetic, and Fano-like resonances (Fig. 4.10A) is formed. The resonances in these structures arise from the strong electromagnetic coupling between closely spaced particles and can be described by plasmon hybridization [36]. Clusters are assembled in a relatively straightforward manner with a capillary-driven method, and their interparticle spacing is controlled by polymer spacers to be ~2 nm, surpassing the spatial resolution of conventional lithography.

Heptamers, which are symmetric clusters composed of seven equivalent elements,

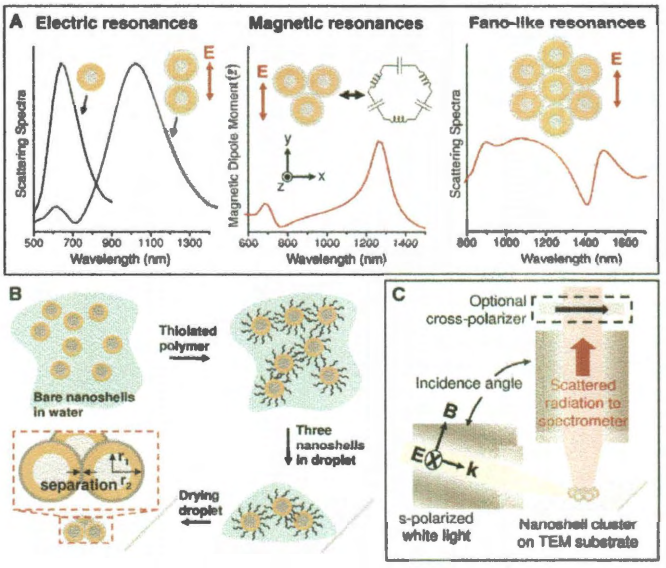

Figure 4.9 : Self-assembled nanoshell clusters as nanoplasmonic components. (A) Nanoshell clusters can be tailored to support tunable electric, magnetic, and Fano-like resonances. Electric dipole resonances generally exist for all plasmonic nanostructures and are shown here for individual nanoshells and coupled dimers. Packed trimer clusters exhibit magnetic dipole resonances and can be described as a closed loop of nanoinductors and nanocapacitors. Fano-like resonances are supported by heptamers. These simulations use nanoshells with $[r_1, r_2] = [62.5, 85]$ nm (where r_1 and r_2 are the inner and outer radii of the gold shell, respectively), and the clusters have 2-nm-wide gaps filled with a dielectric spacer with a dielectric constant $\varepsilon = 2.5$. E, electric field. (B) To assemble the clusters, nanoshells in aqueous solution are coated with a polymer. A dilute droplet of particles is then placed on a hydrophobic substrate and evaporated. During this process, the droplet breaks into smaller droplets, and nanoshells within these smaller droplets pack together by capillary forces. The nanoshell geometry and polymer-spacer separation are defined. (C) To measure scattering spectra, white light is polarized and focused onto the sample, and scattered light from an individual cluster is collected and analyzed in a spectrometer. The optional cross-polarizer is oriented 90° relative to the incident-light polarization. B, magnetic field; k, wave vector of incident light.

support complex plasmon mode interactions that lead to Fano-like interference. Fano-like interference involves a continuum of incident photons (I), a superradiant bright mode (B) that couples to (I), and a subradiant dark mode (D) that does not couple to (I) but instead couples to the bright mode via a near-field interaction. At frequencies resonant with both the bright and dark modes, the former will be excited via two pathways: (i) $|I> \rightarrow |B>$ and (ii) $|I> \rightarrow |B> \rightarrow |D> \rightarrow |B>$. At the Fano minimum, these two pathways destructively interfere and cancel the polarization of the bright mode. The result is a narrow minimum in the scattering and extinction spectra.

The Fano-like resonance is displayed in the calculated extinction spectrum of a heptamer (Fig. 4.10A). The interfering bright and dark modes of the cluster can be characterized by surface charge density plots at their resonances. The charge density plot of the bright mode at its peak at 1160 nm shows the charge oscillations in each nanoshell oriented in the same direction, resulting in strong scattering due to the constructive interference of their radiated fields. The charge density plot at the dark-mode peak frequency at 1490 nm shows only the dark mode, indicating that the bright mode is suppressed and that energy is stored in the dark mode. Here, the charge oscillations in the individual nanoshells are oriented in different directions, resulting in the destructive interference of their radiated fields. Calculations in the quasistatic limit show that the dipole moment of the outer hexagon is similar in magnitude but opposite in sign to the dipole moment of the central particle, leading

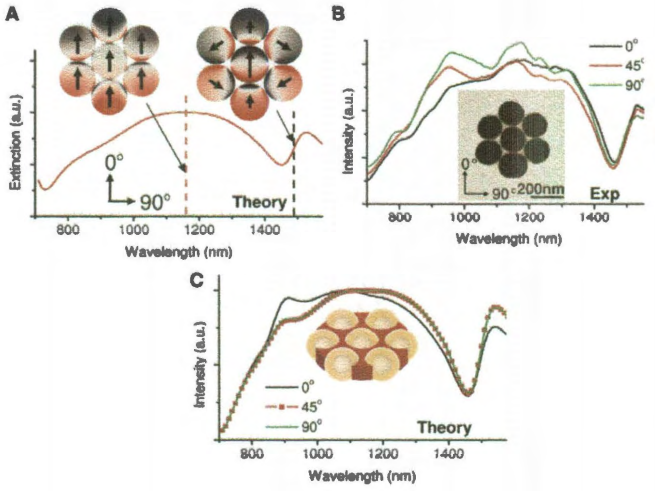

Figure 4.10 : Fano-resonant behavior of a plasmonic heptamer. (A) Calculated extinction spectrum and charge density plots for a heptamer excited at normal incidence with a 0° orientation angle. The nanoshells have dimensions $[r_1, r_2] = [62.5, 85]$ nm, and the cluster has 1.6-nm gap separations and is embedded in a cylinder with a dielectric constant $\varepsilon = 2.5$. The Fano minimum, characterized by suppression of the bright mode, is at 1450 nm. The charge density plot of the bright mode, whose peak resonance is denoted by the pink dashed line at 1160 nm, shows the charge oscillations on each nanoshell oriented in the same direction, resulting in the constructive interference of their radiated fields. The charge density plot of the heptamer at 1490 nm, denoted by the black dashed line, shows the dark mode at its peak resonance. This mode supports charge oscillations on the nanoshells oriented in different directions, resulting in the destructive interference of their radiated fields. (B) TEM image and spectra of a heptamer at three different incident electric-field orientation angles. The nanoshells are measured to have average dimensions $[r_1, r_2] = [62.5, 85]$ nm. The Fano minimum at 1450 nm is isotropic for these orientation angles. (C) Calculated scattering spectra for a heptamer with a geometry matching that in (A), for the three orientation angles in (B).

to strong destructive interference of their radiating fields.

We observe a strong Fano-like resonance in the experimental spectra. The TEM image of a single heptamer and its spectra for three different orientations are shown in Fig. 4.10B. The scattering spectrum at each orientation shows a strong Fano minimum at 1450 nm. This isotropy is consistent with the symmetry of the heptamer (D_{6h} point group), which supports isotropic, in-plane resonances. The peaks between 800 and 1300 nm are higher-order modes that arise from retardation effects created by the large incidence angle. The calculated scattering spectra of a heptamer for different polarization angles are shown in Fig. 4.10C, where the cluster geometry is identical to that used in Fig. 4.10A. These spectra display Fano minima at 1450 nm, with asymmetric line shapes that match the experimental spectra. The nanoshell separation modeled here is smaller than that used for the trimer calculations to account for the strongly red-shifted Fano minimum. This red shift is probably due to a combination of at least three factors: (i) smaller nanoshell separation due to inhomogeneous self-assembled monolayer coverage, (ii) a higher–refractive-index environment near the cluster due to excess polymer deposition, and (iii) increased capacitive coupling between the nanoparticles due to nanoshell faceting.

4.5.2 Gold quadrumers

The TEM image and scattering spectra for an asymmetric quadrumer are presented in Figure 4.11 for different orientations of the incident s-polarized electric field relative

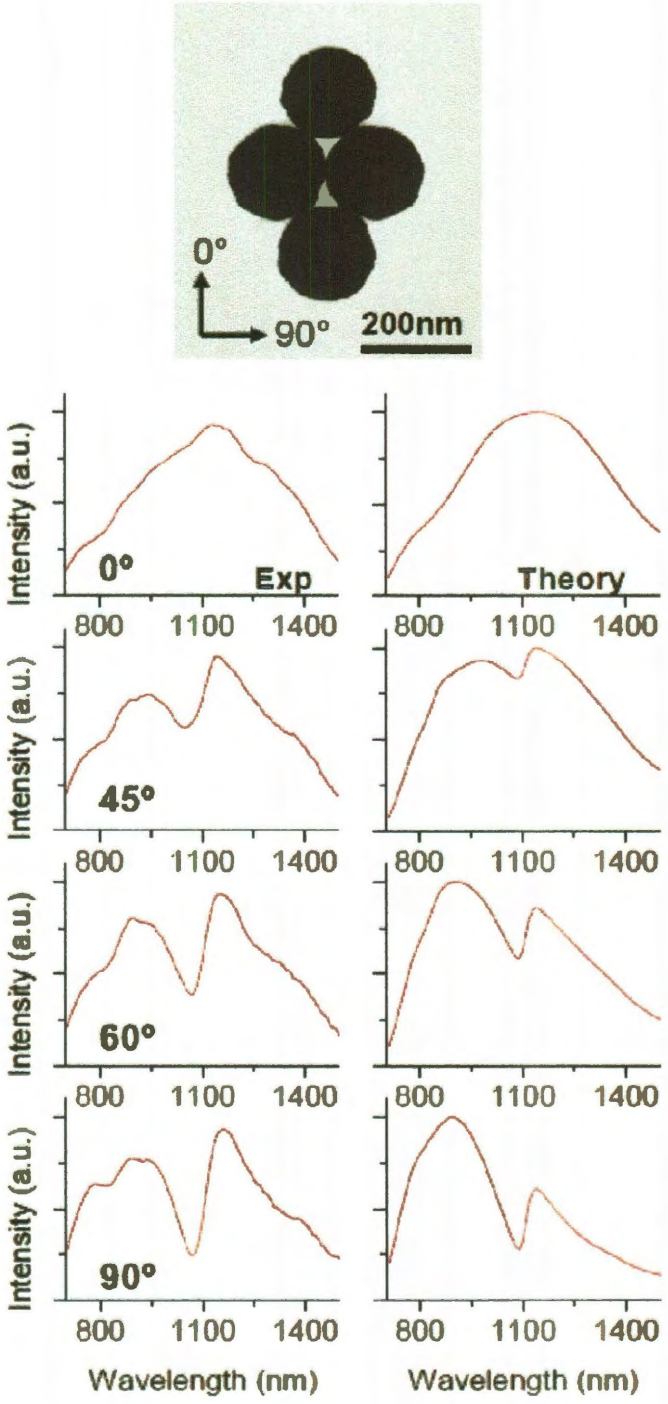

Figure 4.11 : Scattering spectra of the quadrumer(NA=0.64). TEM image and spectra of an asymmetric quadrumer. The orientation angles of the incident electric field relative to the cluster are shown in the TEM image. The experimental spectra show a Fano minimum at 1080 nm that varies with orientation angle and is strongest at 90°. The calculated spectra also show a Fano minimum with a similar resonant wavelength and dependence on orientation angle.

to the cluster. These scattering spectra do not include contributions from absorption. In addition, higher order modes, including the Fano-like dark mode, can couple directly with the incident light due to retardation effects created by the large incidence angle (72° from normal); as a result, higher order mode peaks become visible throughout the spectra, and the Fano-like minimum becomes slightly less pronounced. At 0° orientation, the spectrum shows a smooth, broad electric dipole peak; at 45°, a narrow Fano minimum emerges at 1080 nm, which increases in magnitude for larger orientation angles. Calculated scattering spectra are also plotted in Figure 4.11 and show good agreement with the experimental spectra. As observed experimentally, these spectra display a clear Fano minimum at 1080 nm that is anisotropic with the orientation of the incident electric field.

These quadrumers are modeled with an interparticle separation of 2.0 nm and a nanoshell geometry of $[r_1, r_2] = [62.5, 85]$ nm, where $[r_1, r_2]$ correspond to the silica core and gold nanoshell radii, respectively. These nanoshell geometries are consistent with those from the experimental TEM image. It is difficult to definitively resolve interparticle separations on the order of 2 nm because TEM images are two-dimensional projections of three-dimensional structures; sample properties such as particle faceting and depth-of-field limitations in the TEM image can limit the resolution of this measurement. A spacing of 2.0 nm is chosen by modeling clusters with various separations and choosing the calculated spectra that best matched those from the experiment. It is noted that, while these spacings are small, they are not in a

regime that supports electron tunneling within the gaps, which typically occurs at distances smaller than 1 nm.

4.6 Summaries and conclusions

In this chapter, we have investigated the optical properties of finite clusters of spherical silver nanoparticles. Using group theory we performed a detailed analysis of the plasmon modes in the symmetric pentamer and hexamer. We show that for larger clusters, Fano resonances appear frequently as the result of the interference between super- and subradiant collective cluster plasmon modes. In addition, we show two experimental examples: gold heptamers and gold quadrumers. We show pronounced Fano resonace in gold heptamers structure. We also show that the asymmetric quadrumer cluster supports a pronounced Fano minimum. The strength of this resonance strongly depends on the polarization of incident electric field, which is due to orientation-dependent capacitive coupling within the cluster.

Chapter 5

Silver Nanowire Surface Plasmon Waveguides

5.1 Introduction

Subwavelength photonic devices can be integrated with electronics to overcome the bandwidth and data transmission rate limitations of classical electrical interconnects.[133] The development of such miniaturized photonic circuits is of great current interest in nanophotonics.[134, 135] Plasmonics as a subfield of nanophotonics is concerned with the control of light at the nanoscale, using surface plasmons polaritons (SPPs).[136, 137, 138, 62] As the nanoscale analog of an optical fiber, plasmonic waveguides are an important component needed for light transmission in surface plasmon-based photonic circuitry.[139, 140, 141] Recently various types of plasmonic waveguides have been developed.[61, 142, 143, 144, 145] It has been shown that gold and silver nanowires can guide SPPs up to tens of micrometers with relative low loss of energy.[146, 147, 148, 149, 150] Many studies have focused on improving the performance of the nanowire waveguide, achieving higher in-coupling efficiency of light[149, 151]) and lower propagation loss.[62, 150] However, very little is known about how the polarization of the out-coupled light is related to the polarization of the incident light. An understanding of the input-output polarization properties of light from plasmonic nanowire waveguides is crucial for waveguide design, optical in-

terconnects, and the ultimate integration of active plasmonic devices such as logic elements, switcher, and multiplexers.

Much recent work on plasmonic waveguides has focused on chemically synthesized metallic nanowires, which support plasmon propagation with minimum loss. [146, 151, 152, 147, 148] For efficient plasmonic waveguiding, it is important to minimize the loss inherent in the in- and out-coupling efficiencies between photons and plasmons and during plasmon propagation in the waveguide. [135, 139, 153, 154, 140] Several investigations of loss mechanisms have been performed, [153, 154] but to our knowledge, no previous investigation has addressed the possibilities of loss induced by energy transfer into the substrate. This is clearly an important issue since plasmonic waveguides and devices are almost universally fabricated or deposited on substrates of various dielectric or semiconducting media.

In section 5.2, SPPs are excited at one end of a silver nanowire. While varying the polarization of the excitation beam, the polarization of the light emitted at the other end of the nanowire was analyzed. The polarization change is found to depend sensitively on the geometrical shape of the wire terminations. Theoretical analysis shows that the shape of the nanowire termination where the plasmon is launched determines the relative intensity of the SPPs modes excited in the nanowire, which can modify the polarization of the emitted light. The shape of the emission end, on the other hand, can change both the spatial distribution and polarization of the emitted light. With properly designed nanowire terminations, a nanowire can serve either as a

polarization-maintaining plasmonic waveguide or as a nanoscale polarization rotating half-wave plate.[113, 116]

In section 5.3, we investigate plasmon propagation in Ag nanowires positioned at different separations from dielectric substrates of various compositions. We find that both the incoupling efficiency of light into nanowire SPPs and the damping of the propagating plasmon depend sensitively on the proximity of the nanowire to the substrate and on the dielectric permittivity of the substrate. [155, 156, 157] While the damping of the propagating plasmon decreases monotonically with increasing nanowire-substrate separation, the incoupling efficiency exhibits a surprisingly non-monotonic behavior, peaking at specific nanowire-substrate separations related to the interference between the incident light and reflected light from the substrate. The damping of the propagating plasmon influenced by the substrate can be understood as resulting from interactions between the nanowire and the substrate.

5.2 Correlation between Incident and Emission Polarization in Nanowire Surface Plasmon Waveguides

The experimental setup is shown in Figure 5.1a. A laser beam with the wavelength 633 nm is focused onto one end of a silver nanowire with an objective (Olympus UP-lanApo, 100×, N.A. = 1.35). The polarization of the incident light is rotated by a half-wave plate before the half-reflecting mirror. The emission from the other end of the nanowire is collected by the same objective and recorded by a TE cooled 1392 ×

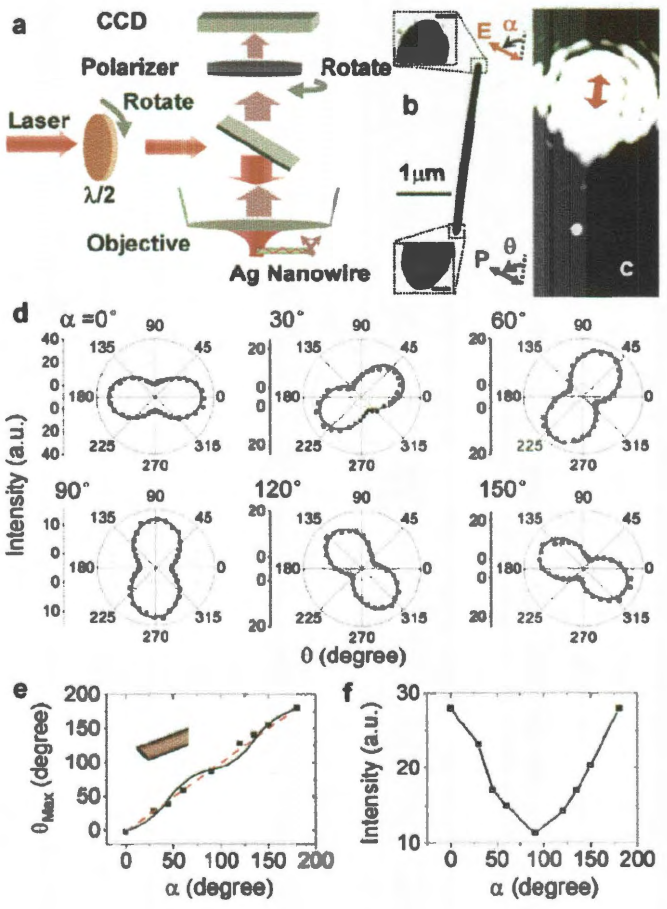

Figure 5.1 : Polarization measurement. (a) Scheme of the experiment. (b) TEM image of a wire of length $3.36\mu m$ and diameter 130 nm. The scale bar in the TEM insets showing the shape of the wire ends is 50 nm. (c) Optical image of the nanowire in a microscope under the excitation of a 633 nm laser spot polarized along the wire. Red arrow indicates the polarization of the laser. (d) Emission intensity as a function of the polarizer rotation angle θ, for different incident polarizations ($\alpha = 0, 30, 60, 90°, 120, 150°$, respectively). The incident polarization and the polarizer are rotated anticlockwise relative to the wire axis, which is defined by the angle α and θ in the inset of (b). (e) Polarization of the emission as a function of the incident polarization. θ_{max} is the polarization angle of the emission defined as the rotation angle of the polarizer when the emission is the maximum. Dots are the measured data. Black curve is the simulation result based on a cylindrical wire with the shape of both ends shown in the inset. The linear dashed red line is drawn to guide the eyes. (f) Maximum emission intensity from the wire as a function of incident polarization angle.

1040 CCD detector. By rotating the polarizer in front of the CCD detector, the polarization of the light emitted from the nanowire can be obtained. The silver nanowires were synthesized by chemical fabrication, which yields highly crystalline nanowires with smooth surfaces.[158] The wires are deposited on an ITO glass substrate and immersed in index matched oil $n = 1.518$ during the measurement.

Figure 5.1b shows the transmission electron microscopy (TEM) image of an Ag nanowire of length $3.36\mu m$ and diameter 130 nm. The shape of the nanowire ends are shown with increased detail in the insets. The angle α and θ correspond to the incident polarization and the rotation of the polarizer, respectively. Both angles are rotated anticlockwise relative to the wire axis. In Figure 5.1c, a bright emission spot can be observed following excitation of SPPs from the incident wire end. Figure 5.1d shows the intensity of the wire emission as a function of the rotation of the polarizer. It is clear that nanowire emission as a function of incident polarization angle is almost always linearly polarized. Hence, the direction of the emission polarization can be defined as the angle θ_{max} when the polarizer is rotated to the emission intensity maximum. The angle θ_{max} as a function of the incident polarization is shown in Figure 5.1e. Here we observe that the emission polarization is proportional to the incident polarization, which means that the nanowire SPPs in this case are polarization-maintaining. In this nanowire, parallel incident polarization ($\alpha = 0°$) results in a 2.5 times larger emission intensity than in the case of perpendicular incident polarization ($\alpha = 90°$) (Figure 5.1f).

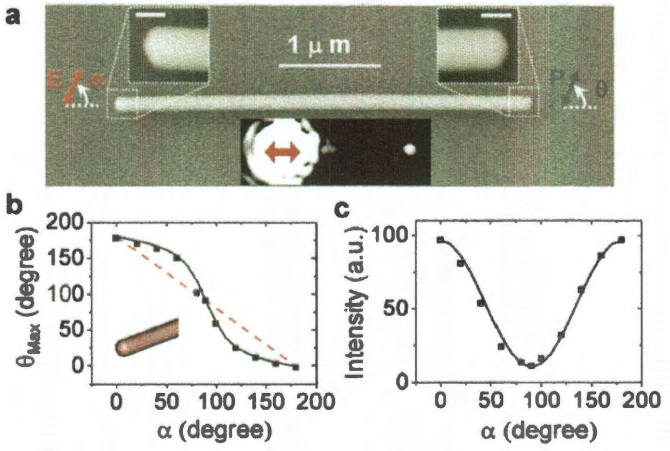

Figure 5.2 : Polarization of emitted light from nanowires. (a) Scanning electron microscopy image of a wire of length $4.54\mu m$ and diameter 148 nm. The scale bar in the insets showing the wire ends is 100 nm. The incident polarization and the polarizer are rotated anticlockwise relative to the wire axis. Inset below: optical image of the wire excited by a parallel polarized 633 nm laser spot at the left end resulting in light emission from the other end of the wire. The red arrow indicates the polarization of the laser. (b) Polarization of the emission as a function of the incident polarization. θ_{max} is the polarization angle of the emitted light. Dots are the measured data. Black curve is the simulation result based on a cylindrical wire with the shape of both terminations shown in the inset. The linear red line is drawn to guide the eyes. (c) Maximum emission intensity from the wire under different the incident polarizations.

The result for another wire is shown in Figure 5.2. The wire has a similar length ($4.54\mu m$) and diameter (148 nm) to the one in Figure 5.1b, but has different end shapes (see the scanning electron microscopy images in Figure 5.2a). As shown in Figure 5.2b, the polarization of the emitted light still depends on the incident polarization. Interestingly, θ_{max} decreases as the incident polarization α increases, which is opposite to the case in Figure 5.1. The emission intensity under different excitation polarizations is shown in Figure 5.2c. Here, parallel excitation results in 9 times stronger wire emission than for the perpendicular case.

To understand the polarization rotation properties of these nanowires, we performed electromagnetic calculations using finite element method (FEM)-based commercial software (COMSOL). We simulated nanowires with the same length and diameter as those in our experiment, successfully reproducing the measured results. This is shown by the black curves in Figures 5.1e and 5.2b, where the shapes of the ends of the simulated nanowires are shown in the inset. The terminations of chemically synthesized crystalline nanowires usually have five {111} facets.[158] Although we cannot precisely reconstruct the shape of the nanowire ends with high accuracy from electron microscopy images, simulations indeed confirm that within a certain range of wire lengths, it is the shape of the nanowire terminations and not the length of the nanowire that determines the polarization of the emitted light. All the termination shapes used in the simulations presented in this paper are consistent with the SEM images.

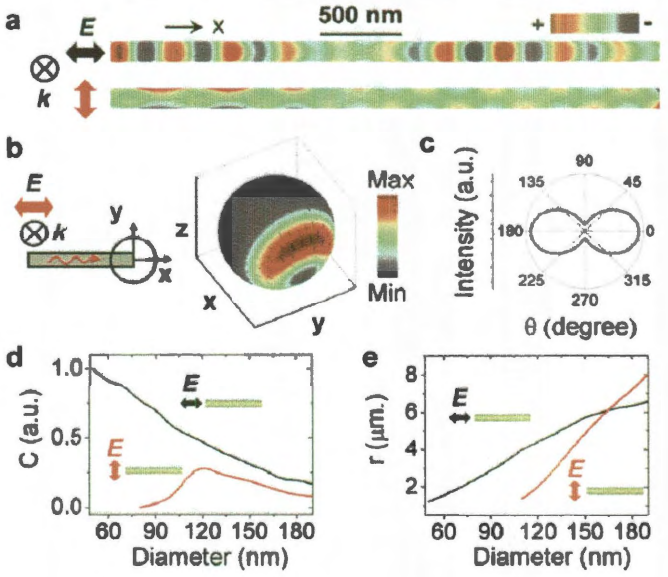

Figure 5.3 : SPPs modes in wires with flat terminations. (a) Charge distribution on the surface of a wire of the length$3.36\mu m$ and diameter 130 nm with flat ends. The left end is excited by a 633 nm focused beam with polarization parallel and perpendicular to the wire, respectively. Colors from red to blue represent charges from positive to negative. (b) The resultant spatial distribution of the emission intensity on a sphere enclosing the wire end excited by the parallel incident polarization. Colors and black lines represent the intensity and the polarization of the emission on the sphere. (c) Emission polarization from the wire excited under the parallel polarized excitation. (d) The in-coupling efficiency C for two SPPs modes (black curve for $m = 0$ mode, red curve for $m = 1$ mode) as a function of the wire diameter. (e) The $1/e$ damping length r of both modes as a function of the wire diameter.

To illustrate the relation between the emission polarization and the shape of the nanowire termination, we first consider a cylindrical nanowire with flat ends. Figure 5.3a shows the charge distribution on the surface of a cylindrical wire with excitation at the left end of the nanostructure. For parallel incident polarization, the fundamental $m = 0$ SPP mode is excited in the wire. For a given position along the wire, the charge density associated with this mode is uniform around the azimuth of the wire. The resulting spatial distribution of the emission intensity on a sphere enclosing the wire end is shown in Figure 5.3b. The $m = 0$ mode will result in parallel polarized emission from the right termination, shown in Figure 5.3c. For perpendicular incident polarization, a transverse charge oscillation is excited, corresponding to the $m = 1$ wire SPP mode. For a given position along the nanowire, the charge density distribution associated with this mode has two nodes around the nanowire azimuth, resulting in a perpendicularly polarized wire emission (not shown). For arbitrary incident polarization, both modes can be excited in the wire, and the polarization of the emitted light is determined by a superposition of emission from the $m = 0$ and $m = 1$ SPP modes. Hence, in any specific nanowire, the polarization of the emitted light is dependent on the relative in-coupling efficiency to the SPP modes and on the damping rate of each mode. By calculating the energy flow of the SPPs excited by the parallel and perpendicular polarization, we fit an exponentially damped energy flow with the formula $Ce^{-x/r}$, where C is the coupling efficiency and r is the $1/e$ damping length of an SPP, respectively, where x is the distance from the excitation

end. For nanowires with diameters D larger than 120 nm, the in-coupling efficiency for the $m = 0$ mode decreases monotonically with increasing D, a result which also has been found by other groups in studies of the coupled dipole-wire system.[159, 160] The in-coupling efficiency for the $m = 1$ mode (red curve) peaks at $D = 120$ nm and then decreases with decreasing D. This decrease in the coupling for thin wires is caused by the effective cut off of the $m = 1$ modes for thin wires where their effective mode volume becomes much larger than the nanowire.[160] The $1/e$ damping length increases monotonically with increasing D for both the $m = 0$ and $m = 1$ modes due to less dissipation for thicker metallic nanowires[160] The damping length of the $m = 1$ mode increases more rapidly than the $m = 0$ mode (Figure 5.3e). For wires with $D < 160$ nm, the $m = 0$ mode is less damped than the $m = 1$ mode. For this reason, excitation with parallel polarization will result in stronger light emission than excitation with perpendicular polarization as shown in Figure 5.2c. This polarization-dependent difference in emission intensity that favors the parallel mode is the reason for the nonlinear input–output polarization characteristic shown in Figure 5.2b. It is important to note that when D is 160 nm or larger, the $1/e$ damping lengths of both $m = 0$ and $m = 1$ modes are of the order of several micrometers. This means that for thick nanowires differing in lengths by several hundreds of nanometers, the relative intensities of the $m = 0$ and $m = 1$ SPP modes will be nearly the same, thus preserving the emission polarization.

The specific shape of the excitation end of the nanowire determines the relative

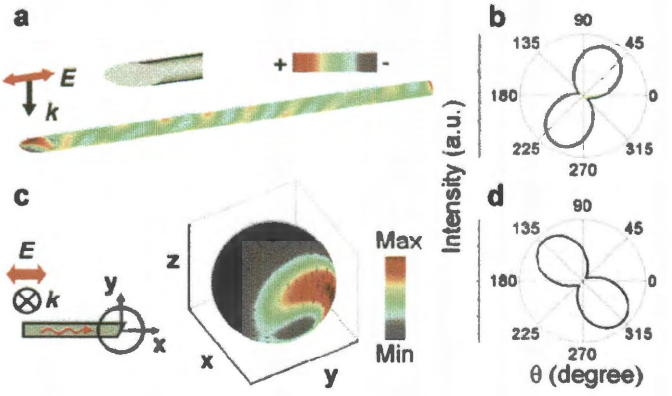

Figure 5.4 : The effect of the termination shape of nanowires on the emission polarization. (a) A 3D view of the charge distribution on the wire surface under the excitation of a parallel polarized beam of wavelength 633 nm. The wire of the length $3.36\mu m$ and diameter 130 nm has a 25° side-cut incident end and a flat emission end as shown in the inset. Colors from red to blue represent charges from positive to negative. (b) Polarization of the emission from the wire in (a) under the parallel polarized excitation. (c) Spatial distribution of the emission intensity on a sphere enclosing the wire end. The cylindrical wire has a flat incident end and a 60° side-cut emission end. The $m = 0$ mode is excited in the wire by a parallel polarized 633 nm laser at the left end. Colors and black lines represent the intensity and the polarization of the emission on the sphere. (d) Emission polarization from the wire in (c) excited under the parallel polarized excitation.

intensity of the two SPP propagating modes, thus strongly affecting the emission polarization. For nanowires with an arbitrary termination shape, both plasmon modes can be excited for arbitrary polarizations. Figure 5.4a shows a three-dimensional (3D) view of the calculated charge distribution on the surface of a cylindrical nanowire with a 25° side-cut incident end excited by parallel polarized light. The charge plot shows that the resulting mode is a superposition of both $m = 0$ and $m = 1$ modes. The polarization of the emitted light is 60° (shown in Figure 5.4b). Conversely, the shape of the emission end also influences the polarization of the emitted light. In Figure 5.4c, a wire with a flat incident end and a 60° side-cut emission end is excited by parallel polarized light. Just as shown in Figure 5.3a, only the $m = 0$ wire SPP mode is excited. Because of the asymmetric shape of the emission end, the spatial distribution of the emission intensity is asymmetric. The polarization of the emission is changed to $-45°$ as shown in Figure 5.4d, rather than parallel to the wire axis. Further theoretical investigation on the emission polarization from wires with various shapes will be presented in a future study.

As demonstrated above, by modifying the shape of the incident wire end, one can control the relative intensities of the two SPP modes launched in the wire. The light emission characteristics will depend both on the relative intensities of the $m = 0$ and $m = 1$ modes reaching the emission end and on the shape of the emission wire terminus. Because of the mode-specific damping lengths of the SPPs, the properties of the emission polarization can depend on the wire diameter and for long wires, the

wire length.

The present study clearly revealed that the major factor influencing the light emission polarization is the shape of the wire terminations. Although chemically synthesized crystalline nanowires usually has five {111} facets,[158] these facets are sometimes not identical, which leads to nanowire terminations of various multifaceted shapes. As a consequence, the emission polarization properties of each nanowire will depend on its particular shape. An extensive investigation of tens of nanowires (a few are presented in the Supporting Information) shows that most of them have emission polarization characteristics that either correlates positively with the incidence polarization or correlates negatively. In rare instances, the emission polarization depends on the incidence polarization in more complex way. To manipulate the polarization of the nanowire emission, we envision that one could reshape the nanowire terminations to desired shapes by techniques such as focused ion or electron beam milling. It is important to note that by controlling the shape of the nanowire terminations it will be possible to selectively fabricate polarization-maintaining or polarization-changing plasmonic waveguides in a controlled manner.

5.3 Effect of a proximal substrate on plasmon propagation in silver nanowires

Chemically synthesized Ag nanowires [158] were deposited on Si substrates with SiO_2 surface spacer layers of varying thicknesses. The nanowire was then embedded in

immersion oil with a refractive index matched to the silica layer. Thus the silica layer is negligible optically and serves only as a passive spacer layer. SPPs are launched at one end of the nanowire by a diffraction-limited 633 nm laser spot focused by an oil immersion objective Olympus UPlanApo, 100, NA=1.35. The polarization of the incident laser is rotated to be parallel to the nanowire axis by a half-wave plate to ensure maximum emission intensity. The emission intensity from the other end of the nanowire is recorded by a TE cooled 13921040 charge-coupled-device detector. The diameter of each nanowire is measured by scanning electron microscopy.

The emission intensities from nanowires of diameter in the range $D = 90-100$ nm, for three separations, are shown in Fig. 30a. It is clearly seen that nanowires of similar lengths on a thick SiO_2 spacer layer $d = 110$ nm usually emit light more strongly than nanowires on a thin layer $d = 67$ nm. For silica layers of thickness less than 41 nm, there is almost no observable emission from the nanowire end. It should be noted that the measured data are still significantly scattered around the fitting line even when the distribution of nanowire diameters is narrowed to $D = 95 - 100$ nm. This scatter is mainly caused by the strong sensitivity of the SPP Fabry-Pérot resonances to slight variations in nanowire diameters and lengths, as reported previously. [161] Various shapes of nanowire terminations can also cause discrepancies in the emission intensity from nanowires with similar length and diameter. [161]

To understand the strong dependence of nanowire emission on spacer layer thickness, we parametrize the emission intensity I_e as

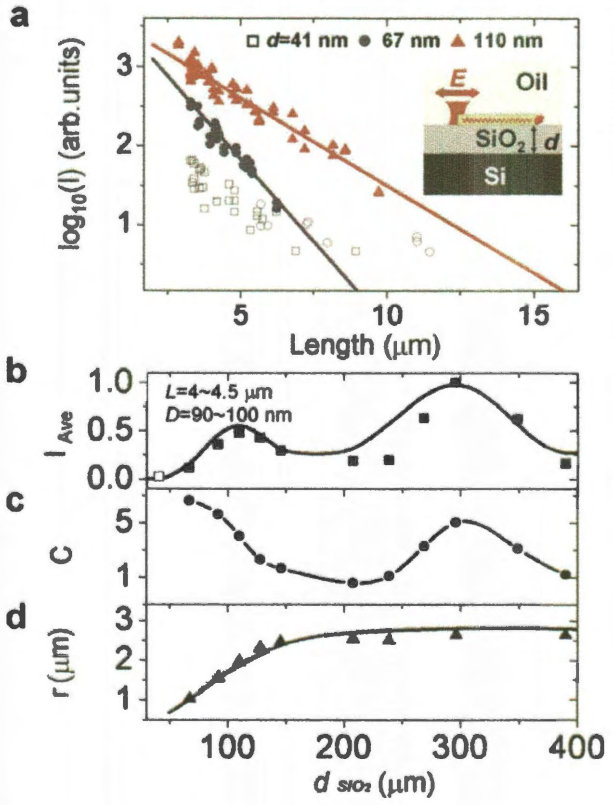

Figure 5.5 : (a) Emission intensities from nanowires on layered substrates as a function of nanowire length L. The diameters of all nanowires were selected to be in the range $D = 90-100$ nm. Inset: a schematic of the experimental measurement. Incident light of wavelength 633 nm, polarized parallel to the nanowire, is directed onto one end of the nanowire. Light emitted from the other end is measured for various nanowire lengths L and silica layer thicknesses d = 41, 67, and 110 nm. When there is no observable light emission, the scattered light at the end of the nanowire is recorded and represented by hollow dots. (b) Average emission intensity for nanowires black squares of length $L = 4 - 4.5\mu m$ and diameter $D = 90 - 100$ nm as a function of the silica layer thickness d. The curve is the theoretical simulation FDTD of this geometry. (c) In-coupling coefficient C as a function of silica thickness d. The unit for I_{Ave} and C in (b) and (c) is arbitrary. (d) $1/e$ damping length of SPPs as a function of d. The curve is the calculated r divided by 1.4, discussed in the text. The refractive index of silicon is 3.882. The refractive of the oil is index matched to silica $n_s = 1.518$.

$$I_e = I_0 C(d) e^{-L/r(D,d)} \tag{5.1}$$

where L is the length of the nanowire, I_0 is the incident intensity, $C(d)$ is the in-coupling coefficient, and $r(D,d)$ is the $1/e$ damping length of the nanowire SPPs.

In Fig. 30b, the average emission intensity from nanowires of similar length $L = 4 - 4.5\mu m$ and diameter $D = 90 - 100$ nm on layered substrates as a function of silica layer thickness d, normalized it to maximum emission in each case, is shown. It is interesting that the average emission intensity exhibits a strongly nonmonotonic behavior, with maxima occurring at $d \sim 110$ and 300 nm, decreasing very strongly as d is reduced to zero thickness. Figures 5.5c and 5.5d show the in-coupling coefficient $C(d)$ and $1/e$ damping length $r(D,d)$ of SPPs in nanowires on layered substrates obtained by fitting the experimental data to Eq. 16. The in-coupling coefficient C is large for $d = 40$ nm, then decreases for increasing d until $d \sim 200$ nm, then increases and peaks for $d \sim 300$ nm, and then decreases. The damping length $r(D,d)$, on the other hand, increases monotonically with increasing silica thickness and saturates beyond $d > 200$ nm. The combined effect of increased in-coupling efficiency but decreased propagation length due to increased substrate coupling for small nanowire-substrate separations leads to an overall maximum in light emission at $d \sim 110$ nm (Fig. 30b).

To understand the effect of the substrate on in-coupling efficiency and propagation length, electromagnetic simulations using finite-difference time-domain FDTD-based

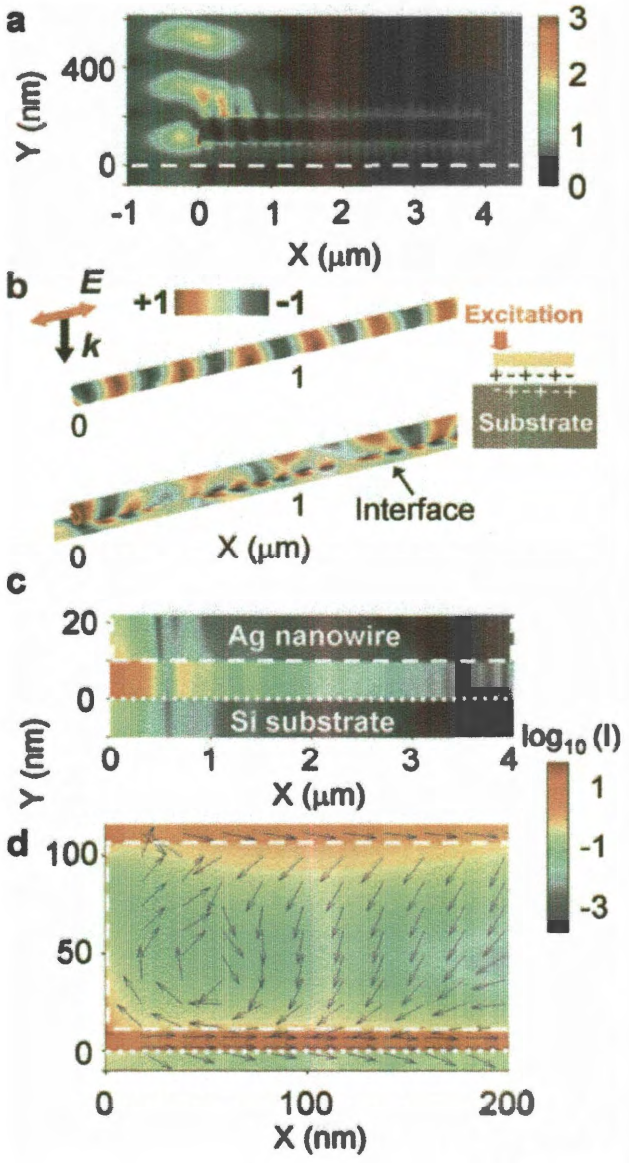

Figure 5.6 : (a) The field distribution $|E|^2$ around the nanowire of diameter 96 nm, length $4\mu m$, and $d = 100$ nm excited by a 633 nm laser with parallel polarization relative to the wire axis at the left end. (b) The plasmon-induced surface charge amplitude on the nanowire without and with adjacent Si surface $d = 10$ nm. The charge is obtained by the divergence of the electric field. The unit of charge is arbitrary from $+1$ to -1 corresponding to color from red to blue. (c) The intensity of the electric field confined in the wiresubstrate gap in (b) on a logarithmic scale. (d) The Poynting vector/electromagnetic energy flow around the first 200 nm of the wire and the wire-substrate gap. Arrows denotes the direction of the flow; the color represents the local electric intensity.

commercial software LUMERICAL were performed. Figure 5.6a shows the field distribution around a nanowire for $d = 100$ nm. It is clear that propagating SPPs are launched along the nanowire. Due to the superposition of the incident and substrate-reflected light, standing waves are formed in the vertical direction y direction. The first two antinodes of standing waves are located at approximately 100 and 300 nm in the y direction. As the thickness of the spacer layer is increased, the excitation end of the nanowire moves across these two antinodes, enabling more efficient in-coupling and thus enhanced light emission Figs. 30b and 30c. The calculated emission intensity from a nanowire of length $L = 4\mu m$ and diameter $D = 96$ nm, shown in Fig. 30b, agrees very well with the experimental data.

For $d < 200$ nm, when the nanowire is close to the Si substrate, the in-coupling coefficient C shown in Fig. 5.6c increases dramatically. Although this means that more light can be coupled to SPPs in the nanowires for larger C, the proximity of the nanowire to the substrate results in significantly more damping, as evidenced by the reduced damping length r shown in Fig. 5.6d.

To understand the strong decrease in propagation length with decreasing spacer layer thickness, we calculate the plasmon-induced surface charge on the surface of a silver nanowire and the induced surface charges at the silicon interface for a thin $d = 10$ nm silica spacer layer Fig. 5.6b. Here the large induced surface charges at the silicon interface represent a strong coupling to the nanowire plasmon, which results in the wavelength of the propagating plasmons being reduced to 200 nm, in

comparison with the case of a free wire without substrate ($\lambda_{plasmons} \sim 320$) nm. The charge distribution in the substrate can confine the plasmon modes in the gap between the nanowire and the silicon surface,[162, 163] as indicated in Fig. 5.6c. Figure 5.6d shows the Poynting vector/electromagnetic energy flow in the gap and wire. It is clear that the photons can propagate in the wire-substrate gap, i.e., that, the gap mode is excited. When d is decreased, the resonance of the gap mode is redshifted and results in larger propagation damping. By calculating the energy flow along the nanowire for different separations, the corresponding SPP damping lengths are extracted and plotted with the black curve in Fig. 30c. The calculated values are about 40% larger than the experimental values. This discrepancy may be caused by uncertainties in the silver dielectric function used in calculation,[57] or may also be due to the presence of defects in the chemically synthesized nanowires. For $d < 40$ nm, the damping of the nanowire plasmons becomes so large that the resulting emission intensity from the nanowire end becomes very weak. This may be the reason why no light emission was detected at the distal end of the nanowire and only the light scattered by the wire end could be detected, as shown by the hollow squares in Fig. 30a. Further analysis shows that the substrate-induced damping length approximately follows the relation, $r = r_0 e^{-\eta^3/d^3}$ in the range of $40 < d < 400$ nm, where r_0 is the SPPs damping length without substrate, $\eta = d_0(\varepsilon - \varepsilon_s)/d_0(\varepsilon + \varepsilon_s)$, where $\varepsilon$and ε_s are the real part of the permittivities of the substrate and of the dielectric surroundings, respectively. The best fit to the experimental data is obtained for $d_0 = 98$ nm.

5.4 Summaries and conclusions

In this chapter, we have investigated the correlation between the incident and emission polarization in plasmonic Ag nanowire waveguides. By combining experiments and simulations, we find that the polarization change depends only slightly on the diameter and length of the wire, but sensitively on the shape of the wire terminations. The shape of incident nanowire end influences the strength of the SPP modes excited on the nanowire, while the shape of the emission end affects the intensity distribution and polarization of the emitted light. Hence, the polarization and intensity of the nanowire emission can be manipulated by modifying the shape of the nanowire termination. Also, we have measured the emission intensity of SPPs launched in individual silver nanowires at different separations from different substrates. We find that both the in-coupling efficiency and the damping length of the nanowire plasmons are influenced by the presence of a nearby substrate. The in-coupling efficiency can exhibit strong peaks for certain wire-substrate separations due to the interference between incident and reflected light. In contrast, coupling to the substrate makes the decay length of nanowire plasmons decrease monotonically with decreasing wire-substrate separation. This coupling depends on wire-substrate separation and the dielectric permittivity of the substrate. For strongly absorbing substrates, the substrate-induced damping can be very large. The understanding of the propagating properties of surface plasmons on substrates is important for the development of nanoscale photonic devices.

Chapter 6

Conclusion

In the thesis, we have generally introduced plasmon hybridization method and shown that this method can be extended to include realistic permittivities for metals and to calculate the plasmon-induced electromagnetic field enhancements and optical spectra. We need to keep in mind that the PH theory itself does not include retardation effect. However, by using the 'modes' concept and 'hybridize' concept, lots of interesting optical properties of noble metallic nanostructures can be explained in a simple and physical way.

With PH method in mind, conbining with Finie Element Method and group theory, we have theoretically investigated optical properties of some complex noble metal nanoparticle aggregates. These aggregates have very promising potentials in applications like biosensing,[58, 59, 60] subwavelength waveguiding,[61, 62] metamaterial applications,[63, 64, 65] imaging and fluorescence applications,[66, 67, 68] and biotechnology.[69, 70, 71] The unique ability of plasmons to focus incident light into subwavelength volumes near metal surfaces can lead to very intense local fields. The field intensities of such hotspots can reach sufficient levels to enable single molecule Surface Enhanced Raman Scattering (SERS).[72] The largest plasmonic field enhancements are typically occurring in junctions between adjacent nanoparticles. Another very hot feature of these nanoparticle aggregates is that larger structures such as

symmetric heptamers or asymmetric quadrumers support very narrow Fano resonances with unusually high spectral sensitivities to the dielectric environment of the nanostructure. Nanostructures supporting strong Fano-like interference have a range of applications. One is nanoscale waveguiding, where the propagation of radiation along a chain of nanostructures at their Fano minimum can yield highly dispersive and relatively scatter-free waveguiding. These structures can also be used as optical cavities because they can store large amounts of energy in the dark mode. Their integration with gain media can lead to light amplification at this mode. An application for individual passive structures is localized surface plasmon resonance (LSPR) sensing, in which shifts in plasmon resonance energy are measured as a function of the refractive index of the environment. Structures supporting Fano-like resonances are ideal for nanoscale LSPR sensing because they are particularly sensitive to the surrounding environment and have relatively narrow linewidths.

We further use the PH method along with numerical simulation method (FEM) to analyze how the plasmon modes propagate along a silver nanowire. We first investigated the correlation between the incident and emission polarization in plasmonic Ag nanowire waveguides. Bothe experiments and simulations show that the polarization change depends only slightly on the diameter and length of the wire, but sensitively on the shape of the wire terminations. The shape of incident nanowire end influences the strength of the SPP modes excited on the nanowire, while the shape of the emission end affects the intensity distribution and polarization of the emitted light.

Next, we have measured the emission intensity of SPPs launched in individual silver nanowires at different separations from different substrates. We find that both the in-coupling efficiency and the damping length of the nanowire plasmons are influenced by the presence of a nearby substrate. The in-coupling efficiency can exhibit strong peaks for certain wire-substrate separations due to the interference between incident and reflected light. In contrast, coupling to the substrate makes the decay length of nanowire plasmons decrease monotonically with decreasing wire-substrate separation. This coupling depends on wire-substrate separation and the dielectric permittivity of the substrate. For strongly absorbing substrates, the substrate-induced damping can be very large. The understanding of the propagating properties of surface plasmons in nanowires is important for the development of nanoscale photonic devices.

Bibliography

[1] I. Angelini, G. Artioli, P. Bellintani, V. Diella, M. Gemmi, a. Polla, and a. Rossi, Journal of Archaeological Science **31**, 1175 (2004). 1

[2] P. Colomban, G. March, L. Mazerolles, T. Karmous, N. Ayed, A. Ennabli, and H. Slim, Journal of Raman Spectroscopy **34**, 205 (2003). 1

[3] P. Colomban, Journal of Nano Research **8**, 109 (2009). 1

[4] S. Perezvillar, J. Rubio, and J. Oteo, Journal of Non-Crystalline Solids **354**, 1833 (2008). 1

[5] W. Fritzsche and T. A. Taton, Nanotechnology **14**, R63 (2003). 2

[6] I. Brigger, C. Dubernet, and P. Couvreur, Advanced drug delivery reviews **54**, 631 (2002). 2

[7] I. H. El-Sayed, X. Huang, and M. a. El-Sayed, Nano letters **5**, 829 (2005). 2

[8] W. Cai, T. Gao, H. Hong, and J. Sun, Nanotechnology, Science and Applications **1**, 17 (2008). 2

[9] J.-L. Li, L. Wang, X.-Y. Liu, Z.-P. Zhang, H.-C. Guo, W.-M. Liu, and S.-H. Tang, Cancer letters **274**, 319 (2009). 2

[10] T. B. Huff, L. Tong, Y. Zhao, M. N. Hansen, J.-X. Cheng, and A. Wei, Nanomedicine (London, England) **2**, 125 (2007). 2

[11] L. Tong, Y. Zhao, T. B. Huff, M. N. Hansen, A. Wei, and J.-X. Cheng, Advanced materials (Deerfield Beach, Fla.) **19**, 3136 (2007). 2

[12] T.-R. Kuo, V. a. Hovhannisyan, Y.-C. Chao, S.-L. Chao, S.-J. Chiang, S.-J. Lin, C.-Y. Dong, and C.-C. Chen, Journal of the American Chemical Society **132**, 14163 (2010). 2

[13] M. S. Yavuz, Y. Cheng, J. Chen, C. M. Cobley, Q. Zhang, M. Rycenga, J. Xie, C. Kim, K. H. Song, A. G. Schwartz, et al., Nature materials **8**, 935 (2009). 2

[14] A. Shiotani, T. Mori, T. Niidome, Y. Niidome, and Y. Katayama, Langmuir : the ACS journal of surfaces and colloids **23**, 4012 (2007). 2

[15] P. Podsiadlo, V. a. Sinani, J. H. Bahng, N. W. S. Kam, J. Lee, and N. a. Kotov, Langmuir : the ACS journal of surfaces and colloids **24**, 568 (2008). 2

[16] S. J. Oldenburg, S. L. Westcott, R. D. Averitt, and N. J. Halas, The Journal of Chemical Physics **111**, 4729 (1999). 2

[17] M. Green, Progress in Photovoltaics: Research and Applications **17**, 183 (2009). 2

[18] Z. Liu, W. Hou, P. Pavaskar, M. Aykol, and S. B. Cronin, Nano letters **11**, 1111 (2011). 3

[19] E. Prodan and P. Nordlander, The Journal of chemical physics **120**, 5444 (2004). 3, 6, 9, 15, 21

[20] J. Petschulat, D. Cialla, N. Janunts, C. Rockstuhl, U. Hübner, R. Möller, H. Schneidewind, R. Mattheis, J. Popp, A. Tünnermann, et al., Optics Express **18**, 4184 (2010). 5

[21] C. Chen, J. A. Hutchison, P. Van Dorpe, R. Kox, I. De Vlaminck, H. Uji-I, J. Hofkens, L. Lagae, G. Maes, and G. Borghs, Small (Weinheim an der Bergstrasse, Germany) **5**, 2876 (2009). 5

[22] H. Liang, Z. Li, W. Wang, Y. Wu, and H. Xu, Advanced Materials **21**, 4614 (2009). 5

[23] C. Mu, J.-P. Zhang, and D. Xu, Nanotechnology **21**, 015604 (2010). 5

[24] M. a. Ochsenkühn, P. R. T. Jess, H. Stoquert, K. Dholakia, and C. J. Campbell, ACS nano **3**, 3613 (2009). 5

[25] L. Yang, H. Wang, B. Yan, and B. M. Reinhard, The journal of physical chemistry. C, Nanomaterials and interfaces **114**, 4901 (2010). 5

[26] E. Encina and E. Coronado, The Journal of Physical Chemistry C **114**, 3918 (2010). 5

[27] J. Ye, P. Van Dorpe, L. Lagae, G. Maes, and G. Borghs, **20**, 465203 (2009). 5

[28] C. Tserkezis, N. Papanikolaou, E. Almpanis, and N. Stefanou, Physical Review B **80**, 1 (2009). 5

[29] J. Zhu, The Journal of Physical Chemistry C **113**, 3164 (2009). 5

[30] N. L. Netzer, R. Gunawidjaja, M. Hiemstra, Q. Zhang, V. V. Tsukruk, and C. Jiang, ACS nano **3**, 1795 (2009). 5

[31] I. Chremmos, Journal of the Optical Society of America. A, Optics, image science, and vision **26**, 2623 (2009). 5

[32] C. Khoury, S. Norton, and T. Vo-Dinh, ACS nano **3**, 2776 (2009). 5

[33] T. Teperik and a. Borisov, Physical Review B **79**, 1 (2009). 5

[34] Y.-F. Chau, M. W. Chen, and D. P. Tsai, Applied optics **48**, 617 (2009). 5

[35] J. M. Montgomery, T.-W. Lee, and S. K. Gray, Journal of Physics: Condensed Matter **20**, 323201 (2008). 5, 21

[36] E. Prodan, C. Radloff, N. J. Halas, and P. Nordlander, Science (New York, N.Y.) **302**, 419 (2003). 6, 57

[37] H. Liu, Y. Liu, T. Li, S. Wang, S. Zhu, and X. Zhang, physica status solidi (b) **246**, 1397 (2009). 6

[38] N. Liu, H. Liu, S. Zhu, and H. Giessen, nature photonics **3**, 157 (2009). 6, 52

[39] A. Moradi, Optics Communications **282**, 3368 (2009). 6

[40] Z. Yuan and S. Gao, Physical Review B **73**, 1 (2006). 6

[41] Z.-J. Yang, Z.-S. Zhang, W. Zhang, Z.-H. Hao, and Q.-Q. Wang, Applied Physics Letters **96**, 131113 (2010). 6

[42] Y. Wu and P. Nordlander, The Journal of chemical physics **125**, 124708 (2006). 9

[43] D. W. Brandl and P. Nordlander, The Journal of chemical physics **126**, 144708 (2007). 9

[44] H. Wang, D. W. Brandl, F. Le, P. Nordlander, and N. J. Halas, Nano letters **6**, 827 (2006). 9

[45] C. M. Dutta, T. a. Ali, D. W. Brandl, T.-H. Park, and P. Nordlander, The Journal of chemical physics **129**, 084706 (2008). 9

[46] P. Nordlander, C. Oubre, E. Prodan, K. Li, and M. I. Stockman, Nano Letters **4**, 899 (2004). 9, 14

[47] D. W. Brandl, C. Oubre, and P. Nordlander, The Journal of chemical physics **123**, 24701 (2005). 9, 14, 15

[48] B. Willingham, D. W. Brandl, and P. Nordlander, Applied Physics B **93**, 209 (2008). 9

[49] D. W. Brandl, N. a. Mirin, and P. Nordlander, The journal of physical chemistry. B **110**, 12302 (2006). 9, 18, 23, 25, 40, 44, 45

[50] Y. Urzhumov, G. Shvets, J. Fan, F. Capasso, D. Brandl, and P. Nordlander, Opt. Express **15**, 14129 (2007). 9, 18, 25

[51] N. a. Mirin, K. Bao, and P. Nordlander, The journal of physical chemistry. A **113**, 4028 (2009). 9, 41, 45, 53, 56

[52] F. Hao and P. Nordlander, Applied Physics Letters **89**, 103101 (2006). 9

[53] P. Nordlander and E. Prodan, Nano Letters **4**, 2209 (2004). 9

[54] F. Le, N. Z. Lwin, J. M. Steele, M. Käll, N. J. Halas, and P. Nordlander, Nano letters **5**, 2009 (2005). 9

[55] F. Le, N. Lwin, N. Halas, and P. Nordlander, Physical Review B **76** (2007). 9

[56] T.-H. Park, N. Mirin, J. B. Lassiter, C. L. Nehl, N. J. Halas, and P. Nordlander, ACS nano **2**, 25 (2008). 9

[57] P. Johnson and R. Christy, Physical Review B **6**, 4370 (1972). 11, 21, 42, 83

[58] S. Lal, N. K. Grady, J. Kundu, C. S. Levin, J. B. Lassiter, and N. J. Halas, Chemical Society reviews **37**, 898 (2008). 18, 40, 85

[59] M. Pelton, J. Aizpurua, and G. Bryant, Laser & Photonics Review **2**, 136 (2008). 18, 85

[60] H. Ko, S. Singamaneni, and V. V. Tsukruk, Small (Weinheim an der Bergstrasse, Germany) **4**, 1576 (2008). 18, 85

[61] S. Lal and S. Link, Nature photonics pp. 641–648 (2007). 18, 65, 85

[62] R. F. Oulton, V. J. Sorger, D. a. Genov, D. F. P. Pile, and X. Zhang, Nature Photonics **2**, 496 (2008). 18, 65, 85

[63] D. Korobkin, Y. Urzhumov, B. Neuner III, C. Zorman, Z. Zhang, I. Mayergoyz, and G. Shvets, Applied Physics A **88**, 605 (2007). 18, 85

[64] A. Christ, O. J. F. Martin, Y. Ekinci, N. a. Gippius, and S. G. Tikhodeev, Nano letters **8**, 2171 (2008). 18, 20, 85

[65] N. Liu, L. Fu, S. Kaiser, H. Schweizer, and H. Giessen, Advanced Materials **20**, 3859 (2008). 18, 85

[66] F. Tam, G. P. Goodrich, B. R. Johnson, and N. J. Halas, Nano letters **7**, 496 (2007). 18, 85

[67] M. Fleischer, C. Stanciu, F. Stade, J. Stadler, K. Braun, A. Heeren, M. Haffner, D. P. Kern, and a. J. Meixner, Applied Physics Letters **93**, 111114 (2008). 18, 85

[68] T. Grosges, D. Barchiesi, T. Toury, and G. Gréhan, Optics Letters **33**, 2812 (2008). 18, 85

[69] C. Liu, C. C. Mi, and B. Q. Li, IEEE transactions on nanobioscience **7**, 206 (2008). 18, 85

[70] J. Zhang, Y. Fu, M. H. Chowdhury, and J. R. Lakowicz, The journal of physical chemistry. C, Nanomaterials and interfaces **112**, 9172 (2008). 18, 85

[71] N. G. Khlebtsov, Quantum Electronics **38**, 504 (2008). 18, 85

[72] D. R. Ward, N. J. Halas, J. W. Ciszek, J. M. Tour, Y. Wu, P. Nordlander, and D. Natelson, Nano letters **8**, 919 (2008). 18, 85

[73] T.-J. Yim, Y. Wang, and X. Zhang, Nanotechnology **19**, 435605 (2008). 18

[74] H. Wei, U. Hå kanson, Z. Yang, F. Höök, and H. Xu, Small (Weinheim an der Bergstrasse, Germany) **4**, 1296 (2008). 18

[75] T. Härtling, Y. Alaverdyan, a. Hille, M. T. Wenzel, M. Käll, and L. M. Eng, Optics express **16**, 12362 (2008). 18

[76] V. Giannini and J. a. Sánchez-Gil, Optics letters **33**, 899 (2008). 18

[77] J. Alegret, T. Rindzevicius, and T. Pakizeh, The Journal of Physical Chemistry C **112**, 14313 (2008). 18

[78] S. Xu, S. Hartvickson, and J. X. Zhao, Langmuir : the ACS journal of surfaces and colloids **24**, 7492 (2008). 18, 40

[79] E. M. Hicks, S. Zou, G. C. Schatz, K. G. Spears, R. P. Van Duyne, L. Gunnarsson, T. Rindzevicius, B. Kasemo, and M. Käll, Nano letters **5**, 1065 (2005). 18

[80] a. O. Pinchuk and G. C. Schatz, Applied Physics B **93**, 31 (2008). 18

[81] M. Hossain, T. Shimada, M. Kitajima, and K. Imura, Langmuir pp. 9241–9244 (2008). 18, 40

[82] W. Luo, W. van der Veer, P. Chu, D. Mills, R. Penner, and J. Hemminger, The Journal of Physical Chemistry C **112**, 11609 (2008). 18

[83] C. H. Liu, M. H. Hong, H. W. Cheung, F. Zhang, Z. Q. Huang, L. S. Tan, and T. S. a. Hor, Optics express **16**, 10701 (2008). 18

[84] L. J. Sherry, S.-H. Chang, G. C. Schatz, R. P. Van Duyne, B. J. Wiley, and Y. Xia, Nano letters **5**, 2034 (2005). 19

[85] F. Hao, P. Nordlander, M. Burnett, and S. Maier, Physical Review B **76**, 1 (2007). 19

[86] F. Hao, Y. Sonnefraud, P. Van Dorpe, S. a. Maier, N. J. Halas, and P. Nordlander, Nano letters **8**, 3983 (2008). 20, 38, 52, 54

[87] S. Zhang, D. a. Genov, Y. Wang, M. Liu, and X. Zhang, Physical Review Letters **101**, 1 (2008). 20

[88] G. Bachelier, I. Russier-Antoine, E. Benichou, C. Jonin, N. Del Fatti, F. Vallée, and P.-F. Brevet, Physical Review Letters **101**, 5 (2008). 20

[89] F. Le, D. W. Brandl, Y. a. Urzhumov, H. Wang, J. Kundu, N. J. Halas, J. Aizpurua, and P. Nordlander, ACS nano **2**, 707 (2008). 20, 23, 40, 41, 45, 52

[90] V. Myroshnychenko, J. Rodríguez-Fernández, I. Pastoriza-Santos, A. M. Funston, C. Novo, P. Mulvaney, L. M. Liz-Marzán, and F. J. García de Abajo, Chemical Society reviews **37**, 1792 (2008). 21

[91] J. Zhao, A. O. Pinchuk, J. M. McMahon, S. Li, L. K. Ausman, A. L. Atkinson, and G. C. Schatz, Accounts of chemical research **41**, 1710 (2008). 21

[92] C. Oubre and P. Nordlander, The Journal of Physical Chemistry B **108**, 17740 (2004). 21

[93] C. L. Garrido Alzar, M. a. G. Martinez, and P. Nussenzveig, American Journal of Physics **70**, 37 (2002). 29

[94] S. W. Bishnoi, C. J. Rozell, C. S. Levin, M. K. Gheith, B. R. Johnson, D. H. Johnson, and N. J. Halas, Nano letters **6**, 1687 (2006). 40

[95] S. Lal, S. Clare, and N. Halas, Accounts of chemical research **41**, 1842 (2008). 40

[96] M. W. Knight and N. J. Halas, New Journal of Physics **10**, 105006 (2008). 40

[97] M. P. Jonsson, A. B. Dahlin, P. Jönsson, and F. Höök, Biointerphases **3**, FD30 (2008). 40

[98] E. R. Encina, E. M. Perassi, and E. a. Coronado, The journal of physical chemistry. A **113**, 4489 (2009). 40

[99] S. D. Liu, Z. S. Zhang, and Q. Q. Wang, Optics express **17**, 2906 (2009). 40

[100] C. Hrelescu, T. K. Sau, A. L. Rogach, F. Jackel, and J. Feldmann, Applied Physics Letters **94**, 153113 (2009). 40

[101] S. Franzen, The Journal of Physical Chemistry C pp. 5912–5919 (2009). 40

[102] M. B. Paula Aldeanueva-Potel,Erwan Faoucher,Ramon A. Alvarez-Puebla,Luis M. Liz-Marzan, Analytical chemistry **81**, 9233 (2009). 40

[103] E. Cubukcu, S. Zhang, Y.-S. Park, G. Bartal, and X. Zhang, Applied Physics Letters **95**, 043113 (2009). 40

[104] C.-J. Heo, S.-H. Kim, S. G. Jang, S. Y. Lee, and S.-M. Yang, Advanced Materials **21**, 1726 (2009). 40

[105] D. Wu, X. Xu, and X. Liu, The Journal of chemical physics **129**, 074711 (2008). 40

[106] C. Radloff and N. J. Halas, Nano Letters **4**, 1323 (2004). 40

[107] C. L. Nehl and J. H. Hafner, Journal of Materials Chemistry **18**, 2415 (2008). 40

[108] L. Yang, B. Yan, and B. M. Reinhard, The journal of physical chemistry. C, Nanomaterials and interfaces **112**, 15989 (2008). 40

[109] F. G. de Abajo, The Journal of Physical Chemistry C pp. 17983–17987 (2008). 40

[110] P. H. C. Camargo, M. Rycenga, L. Au, and Y. Xia, Angewandte Chemie (International ed. in English) **48**, 2180 (2009). 40

[111] S. Marhaba, G. Bachelier, C. Bonnet, M. Broyer, E. Cottancin, N. Grillet, J. Lerme, J. Vialle, and M. Pellarin, The Journal of Physical Chemistry C **113**, 4349 (2009). 40

[112] A. Dhawan, S. J. Norton, M. D. Gerhold, and T. Vo-Dinh, Optics express **17**, 9688 (2009). 40

[113] T. Shegai, Z. Li, T. Dadosh, Z. Zhang, H. Xu, and G. Haran, Proceedings of the National Academy of Sciences of the United States of America **105**, 16448 (2008). 40, 67

[114] Y.-F. Chau, H.-H. Yeh, and D. P. Tsai, Physics of Plasmas **16**, 022303 (2009). 40

[115] K. Lopata and D. Neuhauser, The Journal of chemical physics **130**, 104707 (2009). 40

[116] Z. Li, T. Shegai, G. Haran, and H. Xu, ACS nano **3**, 637 (2009). 40, 67

[117] A. J. Mastroianni, S. a. Claridge, and a. P. Alivisatos, Journal of the American Chemical Society **131**, 8455 (2009). 40

[118] Z. Zhang, a. Weber-Bargioni, S. W. Wu, S. Dhuey, S. Cabrini, and P. J. Schuck, Nano letters **9**, 4505 (2009). 40

[119] J. Yan and S. Gao, Physical Review B **78**, 1 (2008). 40

[120] N. Harris, M. Arnold, and M. Blaber, The Journal of Physical Chemistry C **113**, 2784 (2009). 40

[121] A. Gopinath, S. Boriskina, and B. Reinhard, Opt. Express **17**, 1102 (2009). 40

[122] B. Auguié and W. Barnes, Physical Review Letters **101**, 1 (2008). 41

[123] J. a. Fan, C. Wu, K. Bao, J. Bao, R. Bardhan, N. J. Halas, V. N. Manoharan, P. Nordlander, G. Shvets, and F. Capasso, Science (New York, N.Y.) **328**, 1135 (2010). 41, 53

[124] H. U. I. Wang, D. W. Brandl, P. Nordlander, and N. Halas, Accounts of Chemical Research **40**, 53 (2007). 42

[125] N. Liu, T. Weiss, M. Mesch, L. Langguth, U. Eigenthaler, M. Hirscher, C. Sonnichsen, and H. Giessen, Nano letters **10**, 1103 (2010). 52

[126] M. Tribelsky and B. Lukyanchuk, Physical Review Letters **97**, 1 (2006). 52

[127] N. Liu, L. Langguth, T. Weiss, J. Kästel, M. Fleischhauer, T. Pfau, and H. Giessen, Nature materials **8**, 758 (2009). 53, 56, 57

[128] V. M. Shalaev, W. Cai, U. K. Chettiar, H.-K. Yuan, A. K. Sarychev, V. P. Drachev, and A. V. Kildishev, Optics letters **30**, 3356 (2005). 56, 57

[129] T. J. Yen, W. J. Padilla, N. Fang, D. C. Vier, D. R. Smith, J. B. Pendry, D. N. Basov, and X. Zhang, Science (New York, N.Y.) **303**, 1494 (2004). 56

[130] N. Verellen, Y. Sonnefraud, H. Sobhani, F. Hao, V. V. Moshchalkov, P. Van Dorpe, P. Nordlander, and S. a. Maier, Nano letters **9**, 1663 (2009). 56

[131] K. J. Stebe, E. Lewandowski, and M. Ghosh, Science (New York, N.Y.) **325**, 159 (2009). 57

[132] M. Wheeler, J. Aitchison, J. Chen, G. Ozin, and M. Mojahedi, Physical Review B **79**, 2 (2009). 57

[133] X. Duan, Y. Huang, Y. Cui, J. Wang, and C. M. Lieber, Nature **409**, 66 (2001). 65

[134] R. Kirchain and L. Kimerling, Nature Photonics **1**, 303 (2007). 65

[135] X. Guo, M. Qiu, J. Bao, B. J. Wiley, Q. Yang, X. Zhang, Y. Ma, H. Yu, and L. Tong, Nano letters **9**, 4515 (2009). 65, 66

[136] H. Xu and E. Bjerneld, Physical review letters pp. 4357–4360 (1999). 65

[137] E. Ozbay, Science (New York, N.Y.) **311**, 189 (2006). 65

[138] G. W. Bryant, F. J. Garcia de Abajo, and J. Aizpurua, Nano letters **8**, 631 (2008). 65

[139] W. Barnes, A. Dereux, and T. Ebbesen, Nature **424**, 824 (2003). 65, 66

[140] R. Zia, J. Schuller, A. Chandran, and M. Brongersma, Materials today **9**, 20 (2006). 65, 66

[141] A. L. Falk, F. H. L. Koppens, C. L. Yu, K. Kang, N. de Leon Snapp, A. V. Akimov, M.-H. Jo, M. D. Lukin, and H. Park, Nature Physics **5**, 475 (2009). 65

[142] S. a. Maier, P. G. Kik, H. a. Atwater, S. Meltzer, E. Harel, B. E. Koel, and A. a. G. Requicha, Nature materials **2**, 229 (2003). 65

[143] Z. Li and H. Xu, Journal of Quantitative Spectroscopy and Radiative Transfer **103**, 394 (2007). 65

[144] B. Lamprecht, J. R. Krenn, G. Schider, H. Ditlbacher, M. Salerno, N. Felidj, a. Leitner, F. R. Aussenegg, and J. C. Weeber, Applied Physics Letters **79**, 51 (2001). 65

[145] E. Verhagen, J. a. Dionne, L. K. Kuipers, H. a. Atwater, and A. Polman, Nano letters **8**, 2925 (2008). 65

[146] H. Ditlbacher, A. Hohenau, D. Wagner, U. Kreibig, M. Rogers, F. Hofer, F. Aussenegg, and J. Krenn, Physical Review Letters **95**, 1 (2005). 65, 66

[147] A. W. Sanders, D. a. Routenberg, B. J. Wiley, Y. Xia, E. R. Dufresne, and M. a. Reed, Nano letters **6**, 1822 (2006). 65, 66

[148] a. V. Akimov, a. Mukherjee, C. L. Yu, D. E. Chang, a. S. Zibrov, P. R. Hemmer, H. Park, and M. D. Lukin, Nature **450**, 402 (2007). 65, 66

[149] M. W. Knight, N. K. Grady, R. Bardhan, F. Hao, P. Nordlander, and N. J. Halas, Nano letters **7**, 2346 (2007). 65

[150] A. Manjavacas and F. J. Garcia de Abajo, Nano letters **9**, 1285 (2009). 65

[151] R. Yan, P. Pausauskie, J. Huang, and P. Yang, Proceedings of the National Academy of Sciences of the United States of America **106**, 21045 (2009). 65, 66

[152] Y. Fang, H. Wei, F. Hao, and P. Nordlander, Nano letters **9**, 2049 (2009). 66

[153] J. Dionne, L. Sweatlock, H. Atwater, and a. Polman, Physical Review B **72**, 1 (2005). 66

[154] R. Zia, J. Schuller, and M. Brongersma, Physical Review B **74**, 1 (2006). 66

[155] Z. Wang, Ultramicroscopy **23**, 97 (1987). 67

[156] Y. Yu, Y. Jiang, Z. Tang, Q. Guo, J. Jia, Q. Xue, K. Wu, and E. Wang, Physical Review B **72**, 1 (2005). 67

[157] a. Politano, R. G. Agostino, E. Colavita, V. Formoso, and G. Chiarello, physica status solidi (RRL) Rapid Research Letters **2**, 86 (2008). 67

[158] Y. Sun, B. Mayers, T. Herricks, and Y. Xia, Nano Letters **3**, 955 (2003). 69, 71, 77

[159] S.-D. Liu, M.-T. Cheng, Z.-J. Yang, and Q.-Q. Wang, Optics letters **33**, 851 (2008). 74

[160] D. Chang, a. Sø rensen, P. Hemmer, and M. Lukin, Physical Review B **76**, 1 (2007). 74

[161] Z. Li, F. Hao, Y. Huang, Y. Fang, P. Nordlander, and H. Xu, Nano letters **9**, 4383 (2009). 78

[162] H. Xu and M. Kall, Sensors and Actuators B: Chemical **87**, 244 (2002). 83

[163] M. W. Knight, Y. Wu, J. B. Lassiter, P. Nordlander, and N. J. Halas, Nano letters **9**, 2188 (2009). 83